Chemosphere 266 (2021) 128937

Contents lists available at ScienceDirect

Chemosphere

journal homepage: www.elsevier.com/locate/chemosphere

Taguchi optimization design of diameter-controlled synthesis of multi walled carbon nanotubes for the adsorption of Pb(II) and Ni(II) from chemical industry wastewater

Titus Chinedu Egbosiuba [a, c, d, *], Ambali Saka Abdulkareem [a, d], Jimoh Oladejo Tijani [b, d], Jacinta Ijeoma Ani [a], Vida Krikstolaityte [e, f], Madhavi Srinivasan [f], Andrei Veksha [e], Grzegorz Lisak [e, g, **]

[a] Department of Chemical Engineering, Federal University of Technology, PMB.65, Minna, Niger State, Nigeria
[b] Department of Chemistry, Federal University of Technology, PMB.65, Minna, Niger State, Nigeria
[c] Department of Chemical Engineering, Chukwuemeka Odumegwu Ojukwu University, PMB 02, Uli, Anambra State, Nigeria
[d] Nanotechnology Research Group, Africa Centre of Excellence for Mycotoxin and Food Safety, Federal University of Technology, P.M.B 65, Minna, Niger State, Nigeria
[e] Residues and Resource Reclamation Centre, Nanyang Environment and Water Research Institute, Nanyang Technological University, 1 Cleantech Loop, Clean Tech One, 637141, Singapore
[f] Energy Research Institute @NTU (ERI@N), SCARCE Laboratory, Nanyang Technological University, 50 Nanyang Avenue, Singapore, 639798, Singapore
[g] School of Civil and Environmental Engineering, Nanyang Technological University, 50 Nanyang Avenue, 639798, Singapore

GRAPHICAL ABSTRACT

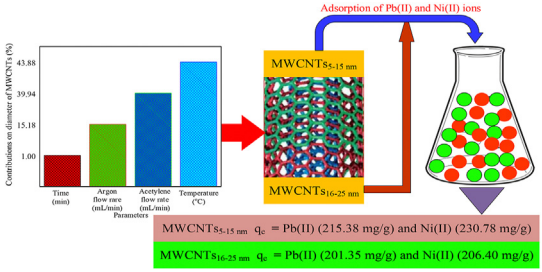

ARTICLE INFO

Article history:
Received 18 September 2020
Received in revised form
5 November 2020
Accepted 7 November 2020
Available online 16 November 2020

Handling Editor: Y Yeomin Yoon

Keywords:
Taguchi optimization
Diameter-controlled carbon nanotubes

ABSTRACT

Herein, Taguchi L_9 orthogonal array was used for the first time to optimize synthesis of diameter-controlled multi walled carbon nanotubes (MWCNTs). The nanoadsorbents, $MWCNTs_{5-15\ nm}$ and $MWCNTs_{16-25\ nm}$ were applied for Pb(II) and Ni(II) ion removal from paint, battery and electroplating wastewater. The results indicated successful synthesis of MWCNTs with diameter distribution ranges of 5 −15 nm and 16−25 nm. The synthetized smaller diameter $MWCNTs_{5-15\ nm}$ revealed higher Brunauer-Emett-Teller (BET) surface area of 1306 ± 5 m^2/g compared to larger diameter $MWCNTs_{16-25\ nm}$with the surface area of 1245 ± 4 m^2/g. They demonstrated excellent adsorption of Pb(II) and Ni(II) ions within the permissible concentration proposed by WHO at pH, contact time, adsorbent dosage and temperature of 5, 60 min, 30 mg/L and 50 °C, respectively. Particularly, $MWCNTs_{5-15\ nm}$ possessed high adsorption capacity of 215.38 ± 0.03 mg/g for Pb(II) and 230.78 ± 0.01 mg/g for Ni(II). Again, the maximum adsorption capacity of 201.35 ± 0.02 and 206.40 ± 0.02 mg/g was achieved for Pb(II) and Ni(II) using

* Corresponding author. Department of Chemical Engineering, Federal University of Technology, PMB.65, Minna, Niger State, Nigeria.
** Corresponding author. Residues and Resource Reclamation Centre, Nanyang Environment and Water Research Institute, Nanyang Technological University, 1 Cleantech Loop, Clean Tech One, 637141, Singapore.
E-mail addresses: ct.egbosiuba@coou.edu.ng (T.C. Egbosiuba), g.lisak@ntu.edu.sg (G. Lisak).

https://doi.org/10.1016/j.chemosphere.2020.128937

Nanoadsorbent
Adsorption
Heavy metal ions

$MWCNTs_{16-25\ nm}$. All in all, the adsorption capacity of the nanoadsorbents at the investigated diameter range showed higher efficiency compared to other materials for heavy metals elimination from chemical industrial wastewater.

1. Introduction

As a result of increasing urbanization and industrialization, a water pollution has been a global concern in the past few decades (Ain et al., 2020). Furthermore, wastewater contamination by heavy metals is largely caused by products and process residues discharged into the environment from various industries, such as paint, chemical, textile, battery, electroplating, metal alloy, leather and ceramic (Qu et al., 2020). Heavy metals such as lead and nickel are considered toxic and are easily assimilated by human body through ingestion, inhalation and dermal contact from/with the polluted water and soil (Mohamed et al., 2019). Particularly, the chronic exposure to lead contamination, in relation to the concentration level of lead and exposure time, may cause adverse changes to the human health which are among others cause plumbism, nervous disorder, memory loss, convulsions, nausea, cerebral disorder, diarrhea, circulatory disorder and could also be fatal at times (Neris et al., 2019). Similarly, the chronic exposure to nickel contamination, in relation to the concentration level of nickel and exposure time, may cause cardiac arrest, pneumonia, brain hemorrhage, liver damage, heart damage, carcinogenic and death (Maddodi et al., 2020). Hence, it is important to treat wastewater and remove the heavy metals to fall within the World Health Organization (WHO) and United State Environmental Protection Agency (US EPA) permissible standard concentration (ranges from 0.05 to 0.1 mg/L for Pb and 0.02–0.07 mg/L for Ni) before reuse or discharge of water to the environment (US EPA, 2012; WHO, 2017).

In the past, various treatment techniques were applied for wastewater purification and removal of Pb(II) and Ni(II) ions, namely adsorption (Oh et al., 2019), chemical oxidation (Oh et al., 2020), biological treatment (Govarthanan et al, 2013, 2018), membrane separation (Yang et al., 2017), chemical precipitation (Georgieva et al., 2020), filtration (Bisheh et al., 2020) and coagulation (Bora and Dutta, 2019). However, most of these methods are ineffective, expensive, requiring longer treatment time and produces highly toxic sludge that needs further treatment. At the moment, adsorption is the most favored alternative for removal of heavy metals as it is highly efficient, it is ease to operate, may be applied on a large scale, offers simultaneous multi-pollutants removal and is cost effective (Egbosiuba et al., 2020a). Recently, carbon nanotubes (CNTs) have attracted interest as an effective adsorbent of heavy metals. Among others, the synthesis of CNTs include arc-discharge (Yatom et al., 2017), laser ablation (Yang et al., 2019) and catalytic chemical vapor deposition (CCVD) (Chen et al., 2020). A major limitation of arc-discharge and laser ablation methods for CNT production are the requirements of high energy and temperature (Chen et al., 2020). The CCVD have gained preferred interests over other synthesis techniques due to its high selectivity, low energy demand, low operation temperature and the production of CNTs of high quality and yield (Malekimoghadam, 2018). To synthesize CNTs by a CCVD, a catalyst, synthesis time, temperature and a carbon source have predominant influence on the quality of CNTs. The ability to control the diameter of the multi walled CNTs (MWCNTs) was found to be crucial for their properties. For example, Yang et al. (2017) have investigated the effect of MWCNT diameter (10–100 nm) towards bacterial toxicity, while Ye et al. (2019) accordingly evaluated the influence of MWCNTs diameter (10–20 nm) as a lubricating additive. Thus, it is of high importance to develop methods that would allow synthesis of different diameter CNTs in a highly controllable approach. In a recent study, Wu et al. (2020) investigated the synthesis of CNTs by CCVD of methane over $Fe@Al_2O_3$ catalysts, which resulted in CNT deposition with diameter ranging from 19 to 58 nm. According to Das et al. (Das and Roy, 2020), diameter-controlled MWCNTs (~15–25 nm) were synthesized by microwave plasma-CVD using chemically processed Fe nanoparticle catalysts. In 2017, Li et al. (2017) reported the development of diameter-controlled MWCNTs over solid ferrocene catalysts which resulted in CNT deposition with diameter of 20–40 nm. Torres et al. (2017) also synthesized MWCNTs with controlled diameter of 8.6 nm by methane catalytic decomposition over Fe–Mo/MgO catalysts. To the best of our knowledge, there are no reports yet available on the diameter-controlled synthesis of MWCNTs using bimetallic Fe–Ni/AC catalysts. In the past few years, studies on Pb(II) and Ni(II) ion removal from industrial wastewater by MWCNT nanoadsorbent are rather scarce.

Over the years, conventional optimization in which a process parameter is varied while other parameters are kept constant is expensive and time consuming. Nevertheless, a more robust technique to optimize several process parameters has been provided by statistical design of experiment (DOE) involving response surface and Taguchi method (Idris et al., 2020). Taguchi optimization method is highly effective in the optimization of multifactor with minimum number of experiments, thereby reducing cost and improving quality (Maazinejad et al., 2020). In this research, L_9 orthogonal array (OA) was utilized to evaluate and optimize the influence of temperature, acetylene flow rate, argon flow rate and time on the diameter distribution of MWCNTs.

Herein, the synthesis of different diameter MWCNTs using bimetallic Fe–Ni catalysts on activated carbon (AC) support in an acetylene environment was studied. The obtained $MWCNTs_{5-15\ nm}$ and $MWCNTs_{16-25\ nm}$ were also characterized by X-ray diffraction (XRD), thermogravimetric analysis (TGA), high resolution scanning electron microscopy (HRSEM), high resolution transmission electron microscopy (HRTEM) and Brunauer-Emmett-Teller (BET). Both, the $MWCNTs_{5-15\ nm}$ and $MWCNTs_{16-25\ nm}$ were investigated for sorption of Pb(II) and Ni(II) ions with practical application of removal of these ions from chemical industrial wastewater.

2. Materials and methods

2.1. Materials

A nitric acid (HNO_3, 98.5% purity), sulphuric acid (H_2SO_4, >98.5% purity), sodium hydroxide (NaOH, >98.5% purity), sodium chloride (NaCl, >98% purity) and calcium chloride ($CaCl_2$, >98% purity) of analytical grade were purchased from Sigma Aldrich. Deionized water was used in this study. An argon and acetylene gases of high purity (>98%) were purchased from British Oxygen Company (BOC Gases) Lagos, Nigeria. The wastewater from paint, battery, electroplating industries was collected from Nnewi industrial layout Anambra, Nigeria. The Fe–Ni/AC catalyst used in this study was

synthesized as reported in our previous work (Egbosiuba et al., 2020b). Briefly, 2.0 and 1.5 g of $Fe(NO_3)_3 \cdot 9H_2O$ and $Ni(NO_3)_2 \cdot 6H_2O$ were placed into a 200 mL conical flask containing 10 g of activated carbon (AC) support and 50 mL of distilled water. The mixture was stirred (150 rpm) for 15 min prior to oven drying of the slurry at 110 °C for 12 h. Afterwards, the sample was cooled to room temperature, grounded and sieved using 150 μm sieve. Subsequently, the catalyst sample was calcined at 400 °C for 6 h to get rid of the moisture and nitrates.

2.2. Synthesis of MWCNTs

In total about 0.6 g of Fe–Ni/AC catalyst was added to a ceramic boat and positioned in the CVD horizontal tube made of quartz. The sample was exposed to argon gas at the heating rate of 50 mL/min until the process temperature of 700 °C was attained. Thereafter, argon flow rate was increased to 100 mL/min, while acetylene gas was switched on at the flow rate of 150 mL/min, and the process continued until the synthesis time of 40 min was achieved as indicated in run 1 of Table S1b. Thereafter, the flow of acetylene gas was discontinued, and the samples slowly cooled down to room temperature under a constant argon gas flow rate of 100 mL/min. After the cooling, the ceramic boat was unmounted from the CVD reactor and the percentage yield of MWCNTs was evaluated using Eq. (1) (Bankole et al., 2018).

$$\text{MWCNTs yield } (\%) = \frac{M_{Total} - M_{catalyst}}{M_{catalyst}} \times 100\% \quad (1)$$

whereby M_{Total} is the mass of MWCNTs after synthesis, while $M_{catalyst}$ is the used mass of Fe–Ni/AC catalyst during the synthesis.

Thereafter, the sample was purified through acid treatment by dissolving 5 g of the MWCNTs in 100 mL of 30% H_2SO_4 and 20% of HNO_3 prior to 3 h sonication. Subsequently, the mixture was continuously washed until a pH of 6 was obtained. Afterwards, the sample was filtered using Whatman grade 1 filter paper, while the obtained wet MWCNT residues were dried at 120 °C for 12 h in an oven.

The diameter distribution of the purified MWCNTs was analyzed using high resolution transmission electron microscope (HRTEM). Similarly, runs 2–9 in Table S1b were carried out using the same experimental procedure when varying experimental conditions. Meanwhile, each of the experiments was repeated in triplicates under the same applied experimental conditions to accurately evaluate the influence of each parameter. The statistical design of an experiment (DOE) involving Taguchi method (Idris et al., 2020; Maazinejad et al., 2020) was applied to synthesize diameter-controlled MWCNTs using bimetallic Fe–Ni/AC catalysts in an acetylene environment. For that Taguchi design of an experiment was utilized to evaluate and optimize the influence of temperature, acetylene flow rate, argon flow rate and time on the diameter distribution of MWCNTs. For each of these factors, three levels (L) of the process parameters (temperature, acetylene flow rate, argon flow rate and time) were also investigated as shown in Table S1a. The initial values for the respective levels of the process parameters were obtained through literature review and preliminary experiments. The calculation of the minimum number of experimental runs were achieved for the 3^4 experimental matrix using Eq. (2). Hence, nine experimental runs (L_9) were performed, the L_9 (3^4) orthogonal array (OA) matrix as shown in Table S1b. The Taguchi experimental design was statistically analyzed using Minitab 18 software.

$$N = (L-1)P + 1 \quad (2)$$

where N refers to the smallest probable number of experimental runs, while P and L are the numbers of process parameters and levels, respectively.

The evaluation of a signal to noise ratio (SNR) from the responses of the Taguchi experimental runs described the ratio of the average diameter of MWCNTs to the standard deviation. In general, the SNR measures the deviation of the quality characteristics from the desired value, whereby signal represents the desired value and noise, the undesired value. More so, the SNR value indicates the scatter near the desired value. Consequently, three types of the SNR were widely explored in statistical approach, depending on the desired quality responses and they accordingly include: smaller is preferential (Eq. (3)), nominal is preferential (Eq. (4)) and bigger is preferential (Eq. (5)) (Kadir Yesilyurt and Cesur, 2020).

$$SNR_S = -10\log\left(\frac{\sum_{j=1}^{n} y_j^2}{n}\right) \quad (3)$$

$$\text{SNR}_S = 10\log\left(\frac{\bar{y}_j^2}{s_j^2}\right) \quad (4)$$

$$SNR_L = -10\log\left(\frac{\sum_{j=1}^{n} 1/y_j^2}{n}\right) \quad (5)$$

The representations of parameters in SNR_N are defined in Eqs. (6) and (7) (Kadir Yesilyurt and Cesur, 2020).

$$\bar{y} = \left(\frac{\sum_{j=1}^{n} y_{i,j}}{n}\right) \quad (6)$$

$$s_j^2 = \left(\frac{\sum_{j=1}^{n} y_{i,j} - \acute{y}_i}{n-1}\right) \quad (7)$$

where y_j is the response parameter, $\bar{y}$ represents the response mean value, s_j^2 is the variance, i is the experiment number, j is the trial number and n refer to the number of trials.

The mean values of the SNR for various samples at the defined experimental conditions were evaluated for each MWCNT synthesis parameter using the OA to report the effect of each parameter on the SNR at different levels.

The contribution factor of the process parameters and their influence on the diameter-controlled synthesis of MWCNTs was investigated by analysis of variance (ANOVA). The degree of freedom of parameter A (DOF_A), sum of squares of parameter (SS_f), total sum of squares (SS_T), mean of square (MS) and the contribution percentage of parameters (P) were evaluated using Eqs. (8–12) (Mojaver et al., 2020).

$$DOF_A = k_A - 1 \quad (8)$$

$$\text{SS}_\text{f} = \sum_{\text{i}=1}^{3} \left[\text{n}(\text{SNR}_\text{S})_\text{fj} - \text{SNR}_\text{T}\right]^2 \quad (9)$$

$$SS_T = \sum_{i=1}^{9} (SNR_i - SNR_T)^2 \quad (10)$$

$$MS = \frac{SS}{DOF} \quad (11)$$

$$P(\%) = \frac{SS_f}{SS_T} X100 \quad (12)$$

where k_A denotes the number of levels for the parameter A.

The obtained MWCNTs were investigated for the adsorption of Pb(II) and Ni(II) from industrial wastewater.

2.3. Material characterization

The MWCNT crystalline structure was analyzed using X-ray diffraction (XRD, 6000, Shimadzu Scientific). The thermal stability of the nanoadsorbents was examined using thermogravimetric analysis (TGA, PerkinElmer, UK). The morphological analysis was performed by high resolution scanning electron microscopy (HRSEM, Zeiss Auriga). The MWCNTs were characterized for their microstructure dimensions using high resolution transmission electron microscope (HRTEM, Zeiss Auriga). The surface area of the MWCNTs was examined using Brunauer-Emmett-Teller (BET, NOVA4200e, Quantachrome UK). The point of zero charge (PZC) was determined by the titration, where 0.04 g of MWCNTs were added to deionized water. The pH meter (Eutech Instruments) was utilized for the determination of solution charge density, while the 0.05 M of HNO_3 and NaOH was used to adjust the surface charge of MWCNTs in the pH range of 2–8 until a zero charge density was obtained.

2.4. Adsorption studies of Pb(II) and Ni(II) ions

Prior to the investigation of Pb(II) and Ni(II) adsorption from industrial wastewater using $MWCNTS_{5-15\ nm}$ and $MWCNTS_{16-25\ nm}$, the initial concentration (C_o) of the metal ions was examined by atomic adsorption spectrophotometer (AAS, PG 990, PG Instruments, UK). The adsorption of Pb(II) and Ni(II) ions from industrial wastewater was conducted in a batch adsorption system while investigating the parameters such as pH, contact time, adsorbent dosage and temperature. In this study, solution pH was investigated in the range of 2–7, whereas contact time was varied from 10 to 180 min. In addition, adsorbent dosage was investigated in the range of 10–60 mg/L, while temperature was studied in the range of 25–50 °C. The supernatants in this study were prepared using classical optimization technique in a water bath (SB25-12DT, Scientz). The required adsorbent dosage (10, 20, 30, 40, 50 and 60 mg/L) was added to 100 mL of Pb(II) and Ni(II) solution under continuous stirring (300 rpm) in a water bath at 25 °C. At the completion of each adsorption experiment, Whatman grade 1 filter paper was used to filter the mixtures and the supernatants analyzed for equilibrium concentration (C_e) of the metal ions by AAS method. Each adsorption experiment was repeated three times and the uncertainties of the measurements in form of the standard deviation were recorded (n = 3). The percentage removal (%) and adsorbed amount (q_e (mg/g)) of Pb(II) and Ni(II) were calculated using Eqs. (13) and (14) (Miyah et al., 2018).

$$\%Removal = \frac{C_0 - C_e}{C_0} x100 \quad (13)$$

$$q_e = \frac{(C_0 - C_e)}{m} xV \quad (14)$$

where C_0 (mg/L) and C_e (mg/L) are the initial and equilibrium concentrations of Pb(II) and Ni(II) in the solution. The V (mL) is the volume of wastewater solution and m (mg/L) is the adsorbent mass.

Furthermore, the impact of competing ions was examined by adding 30 mg/L each of $MWCNTs_{5-15\ nm}$ and $MWCNTs_{16-25\ nm}$ into a conical flask of 0.25 L containing 0.10 L of industrial wastewater. In addition, NaCl and $CaCl_2$ were added to the conical flask using concentrations of 0.1–1.0 mol/L and the mixtures were subjected to the temperature (50 °C) and pH (5) for 60 min under continuous stirring. Afterwards, Whatman grade 1 filter paper was used to filter the mixture and the filtrate analyzed for Pb(II) and Ni(II) ion concentration using AAS.

Additionally, the regeneration of $MWCNTs_{5-15\ nm}$ and $MWCNTs_{16-25\ nm}$ was studied by using 0.1 M HNO_3. Particularly, the adsorbent regeneration was carried out by adding 30 mg/L of spent nanoadsorbents to 100 mL of HNO_3 solutions and stirred (200 rpm) at the temperature of 50 °C for 3 h. Subsequently, the mixture was filtered using Whatman grade 1 filter paper. The adsorption/desorption performance of the nanoadsorbents were repeated six cycles, while the adsorption efficiency (η) evaluated after each cycle using Eq. (15) (Qu et al., 2020).

$$\eta = \frac{C_o - C_e}{C_o} \times 100\% \quad (15)$$

where C_o and C_e (mg/L) represents the initial and equilibrium concentration of Pb(II) and Ni(II) in the solution, respectively.

To further study the isotherm, Langmuir model (Eq. (16)) (Langmuir, 1918), Freundlich model (Eq. (17)) (Oh et al., 2019), Temkin model (Eq. (18) (Zhang et al., 2020) and Dubinin-Radushkevich (D-R) model (Eq. (19)) (Su et al., 2020) were fitted into the experimental data.

$$\frac{C_e}{q_e} = \frac{1}{K_L q_m} + \frac{C_e}{q_m} \quad (16)$$

$$Inq_e = In\ K_F + \frac{1}{n_F} InC_e \quad (17)$$

$$q_e = BInK_t + BInC_e \quad (18)$$

$$Inq_e = Inq_s - k_{DR}\varepsilon^2 \quad (19)$$

in which C_o (mg/L) and C_e (mg/L) are the initial and equilibrium Pb(II) and Ni(II) concentrations. q_e (mg/g) and q_m (mg/g) are the equilibrium and maximum adsorption capacities, respectively. k_L (L/mg) is the Langmuir adsorption constant, while R_L is the separation coefficient. n_F and K_F (mg/g) are the Freundlich adsorption constants, B is the constant correlated to the heat of adsorption (also equal to the slope obtained by fitting the model), K_t is the equilibrium binding constant (L/mg), q_s (mg/g) is the adsorption capacity. K_{DR} refers a constant related to the mean free energy of adsorption per molecule of the adsorbate, while ε (kJ/mol) is a Polyani potential.

In order to achieve successful quantitative description of Pb(II) and Ni(II) ions removal by the nanoadsorbents at the optimum pH, contact time, adsorbent dosage and temperature, pseudo-first order model (Eq. (20)), pseudo-second order model (Eq. (21)), Elovich model (Eq. (22)) and intraparticle diffusion model (Eq. (23)) were utilized to fit the adsorption data (Ho, 2006; Qu et al., 2020; Zhang et al., 2020).

$$In(q_e - q_t) = Inq_e - k_1 t \quad (20)$$

$$\frac{t}{q_t} = \frac{1}{k_2 q_e^2} + \frac{t}{q_e} \quad (21)$$

$$q_t = \left(\frac{1}{\beta}\right) In(\alpha\beta) + \left(\frac{1}{\beta}\right) Int \quad (22)$$

$$q_t = k_3 t^{1/2} + C \quad (23)$$

where q_e (mg/g) and q_t (mg/g) denote the quantity of Pb(II) and Ni(II) ions adsorbed at equilibrium and at time t, respectively. k_1 (min^{-1}), k_2 (g $mg^{-1}min^{-1}$), k_3 (mg $g^{-1}min^{-1/2}$) and α (g $mg^{-1}min^{-2}$) are the equivalent adsorption rate constants, while β (mg $g^{-1}min^{-1}$) and C are the surface coverage coefficient and the boundary layer thickness obtained as the intercept.

Thermodynamic parameters such as standard free energy (ΔG°), enthalpy (ΔH°) and entropy (ΔS°) were evaluated to further determine the adsorption mechanism and explore temperature impact on adsorption of Pb(II) and Ni(II) ions by $MWCNTs_{5-15\ nm}$ and $MWCNTs_{16-25\ nm}$. The thermodynamic parameters were calculated using Van't Hoff relationship as shown in Eqs. (24) and (25) (Qu et al., 2020).

$$\Delta G^\circ = -RTInk_d \quad (24)$$

$$\mathrm{Ink_d} = \frac{\Delta S^\circ}{R} - \frac{\Delta H^\circ}{RT} \quad (25)$$

where k_d (dimensionless) represents the thermodynamic equilibrium constant and is equivalent to $\frac{q_e}{C_e}$. R and T are the universal gas constant (8.314 JK^{-1} mol^{-1}) and temperature (K), respectively. Also, ΔH° (kJ mol^{-1}) and ΔS° (kJ K^{-1} mol^{-1}) were evaluated from the slope and intercept value of a linear plot of In $\frac{q_e}{C_e}$ versus $\frac{1}{T}$ respectively.

3. Results and discussion

3.1. Taguchi optimization of diameter-controlled synthesis of MWCNTs

Taguchi OA technique was applied to investigate the interdependent effect of various parameters such as temperature, acetylene flow rate, argon flow rate and time of the synthesis on the diameter of MWCNTs. The variation of the diameter of CNTs was attained through controlled synthesis and statistical approach, with thinner MWCNTs being preferential as nanoadsorbents for heavy metal adsorption due to the previously reported efficiency of smaller diameter MWCNTs in endothelial cells and lubricants additive (Ye et al., 2019; Zhao et al., 2019). Overall, the highest yield of MWCNTs (Eq.) obtained in this study was 172% as shown in Table 1a. The purification of the obtained MWCNTs revealed effective removal of the metallic impurities and amorphous carbon as shown by the results of the HRTEM (1a-i) and HRSEM (Fig. 2(c,d)). The detailed experimental results of the L_9 OA Taguchi design are indicated in Table S2, while the average diameter (D_{av}) obtained from measured HRTEM images are shown in Fig. 1(runs 1–9). In all, over 100 CNTs were measured for each image in order to obtain a statistically representative value of the measurements. In addition, the values of the SNR_S are shown in Table 1a.

According to the analyzed results with smaller SNR mode being preferential, the lowest MWCNTs diameter was found to be 9.10 nm (Fig. 1(h).), whereas the highest diameter of MWCNTs was determined as 22.00 nm (Fig. 1(f).). The optimal diameter of MWCNTs was identified as showed in Fig. 1(h); however, the set of parameters corresponding to the experiment number may not have been the optimal for the thinner MWCNTs. For this purpose, it was paramount to evaluate the signal to noise ratio level (SNRL) to ascertain the optimum parameters for the synthesis of thinner MWCNTs. In general, the SNRL is defined as the algebraic mean of all SNR of a specific process parameter at a particular level (Kadir Yesilyurt and Cesur, 2020). For example, the SNRL for temperature was obtained as −21.55 for level 1 (Table 1b), which corresponds to the SNR data (−6.52, −6.67 and −8.37) and experiment number 1, 2 and 3. Likewise, the SNRL of temperature for levels 2 and 3 was computed as −26.25 and −23.38 which were also determined as the algebraic mean of the level 2 (−8.67, −8.63 and-8.95) and 3 (−8.10, −6.40 and −8.89) SNR data.

Table 1b illustrates the computed values of SNRL for acetylene flow rate, argon flow rate and synthesis time. The selection of optimum parameters was based on the lowest SNR with respect to each parameter at a specified level. In other words, the delta which is referred to as the difference between the maximum SNRL and the minimum SNRL for each parameter (Idris et al., 2020) was evaluated and presented in Table 1b. The rank defines the contributions of the process parameters in accordance with the delta values from high to low (Sahithi et al., 2019). Consequently, temperature with the maximum delta value (4.70) was ranked 1, while synthesis time with the lowest delta value (0.60) was ranked 4. Overall, the ranking of the parameters in their sequential order of influence on the controlled diameter of MWCNTs were as follows; temperature > acetylene gas > argon gas > time.

The means (averages) estimation of the influence of process parameters on the diameter of MWCNTs are summarized in Table 1c. The results show that temperature had the highest delta value (8.07), thereby exerting most significant effect on the diameter distribution of MWCNTs. Conversely, time had the smallest delta value (1.21) and ultimately had an insignificant influence on the diameter of MWCNTs. The order of the mean values of the parameters is shown in Table 1c. The order was as follows: temperature > acetylene gas > argon gas > time. The observed significant influence of temperature on the controlled diameter of MWCNTs was most likely attributed to the increase in carbon source diffusion rate and solubility on the metallic oxides surface (Yang et al., 2019). In addition, acetylene flow rate remarkably enhanced the deposition of carbon species on the Fe−Ni/AC catalyst surface. Similarly, argon flow rate serving as the carrier gas also enabled the decomposition of carbon source, while synthesis time aided the deposition of the carbon source at the desired temperature and gas flow rates.

The correlation of the main effects of the four process parameters at three levels for the mean of SNR and mean diameter of MWCNTs are presented in Fig. S1(a,b). The graph revealed that there was a sharp increase on the effects of temperature and acetylene flow rate compared to argon flow rate and time because a higher value of SNRL indicate a huge influence of a particular parameter at that specified level (Idris et al., 2020). In addition, the optimum conditions for diameter-controlled synthesis of MWCNTs were defined by the highest SNRL in each graph. As shown in Fig. S1(a,b), a reference line marking the grand mean of the diameter distribution of MWCNTs illustrates the variations of response at different level for each parameter. Particularly, the greatest effect of process parameters in the diameter distribution of MWCNTs was also demonstrated by farthest the main effect line from the reference line. In the graph, temperature had the greatest degree of influence on the diameter distribution of MWCNTs, followed by acetylene flow rates. Furthermore, argon flow rate had a great

Table 1
Results of (a) the average diameter D_{av} of MWCNTs, SNRs and SNR_T values for the L_9 OA of Taguchi design of experiments, (b) SNR analysis for controlled diameter of MWCNTs, (c) response for means of controlled diameter of MWCNTs and (d) ANOVA.

a.

Run	Temperature (°C)	Acetylene flow rate (mL/min)	Argon flow rate (mL/min)	Time (min)	Yield (%)	D_{av} (nm)	SNR_S
1	700	150	100	40	97	9.5	−6.52
2	700	200	150	50	119	10	−6.67
3	700	250	200	60	130	18	−8.37
4	750	150	150	60	155	20	−8.67
5	750	200	200	40	124	19.7	−8.63
6	750	250	100	50	166	22	−8.95
7	800	150	200	50	138	16.4	−8.10
8	800	200	100	60	172	9.1	−6.40
9	800	250	150	40	145	21.5	−8.89
SNR_T = overall mean							−7.91

b.

Level	Temperature (°C)	Acetylene flow rate (mL/min)	Argon flow rate (mL/min)	Time (min)
1	−21.55	−23.29	−21.86	−24.03
2	−26.25	−21.69	−24.23	−23.72
3	−23.38	−26.20	−25.10	−23.44
Delta (max-min)	4.70	4.51	3.24	0.60
Rank	1	2	3	4

c.

Level	Temperature (°C)	Acetylene flow rate (mL/min)	Argon flow rate (mL/min)	Time (min)
1	12.50	15.30	13.53	16.91
2	20.57	12.93	17.18	16.13
3	15.68	20.51	18.03	15.70
Delta (max-min)	8.07	7.58	4.50	1.21
Rank	1	2	3	4

d.

Parameters	DOF	Sum of squares	Mean square	P (%)
Temperature (°C)	2	99.07	49.54	43.88
Acetylene gas (mL/min)	2	90.15	45.08	39.94
Argon gas (mL/min)	2	34.26	17.13	15.18
Time (mins)	2	2.26	1.13	1.00
Error	0	–	–	–
Total	8	225.74	112.88	100

magnitude that is ascribed to its influence on the diameter of MWCNTS and represented the third ranked parameter influencing the diameter of MWCNTs. On the other hand, synthesis time main effect line was very close to the reference line and as such had the least significant influence on the diameter distribution of MWCNTs. In this study, the optimum conditions for the diameter distribution of MWCNTs minimization were obtained as temperature (800 °C), acetylene flow rate (200 mL/min), argon flow rate (100 mL/min) and time (60 min).

3.1.1. Analysis of variance (ANOVA)

Further statistical tests using ANOVA revealed the contributions of temperature, acetylene flow rate, argon flow rate and time on the diameter of MWCNTs. Table 1d shows the ANOVA results for the diameter distribution of MWCNTs where the DOF, SS, MS and percentage contributing parameter were examined. As shown in Table 1d, temperature had most significant influence on the diameter of MWCNTs with the following data: SS (99.07), MS (49.54) and % contribution (43.88%). Acetylene flow rate was the second most influential parameter with SS (90.15), MS (45.08) and % contribution (39.94%), while argon flow rate followed with SS (34.26), MS (17.13) and % contribution (15.18%). Among the process parameters, synthesis time was the least effective process parameter having SS (2.26), MS (1.13) and % contribution (1%) on the diameter distribution of MWCNTs.

3.1.2. Confirmation test on synthesis of diameter-controlled MWCNTs

It was necessary to carry out the confirmation tests to verify the use of Taguchi approach (Ghosh and Mondal, 2019). Table S3 shows the analysis of the initial experimental conditions and the result of Taguchi prediction. As shown, the MWCNT diameter of 9.10 nm were obtained at the temperature (800 °C), acetylene flow rate (200 mL/min), argon flow rate (100 mL/min) and time (60 min). Correspondingly, the MWCNT diameter of 5.92 nm were predicted at the temperature (800 °C), acetylene flow rate (200 mL/min), argon flow rate (100 mL/min) and time (60 min). The close correlation of the experimental and predicted results significantly confirmed the influential degree of these parameters on the diameter-controlled synthesis of MWCNTs.

3.2. Characterization of MWCNTs

Based on the evaluation of diameter distribution of the synthesized MWCNTs (Table S2), the diameter ranges of nanoadsorbents were classified into $MWCNTs_{5-15\ nm}$ and $MWCNTs_{16-25\ nm}$. The nanoadsorbents were characterized using XRD, TGA, HRSEM, HRTEM and BET.

In Fig. 2(a), the XRD patterns for the examination of phase purity and crystalline nature of the $MWCNTs_{5-15\ nm}$ and $MWCNTs_{16-25\ nm}$ were presented. It is apparent in Fig. 2(a) that both nanoadsorbents were crystalline due to the characteristic strong diffraction peaks at 26°, 44° and 50° indicating the

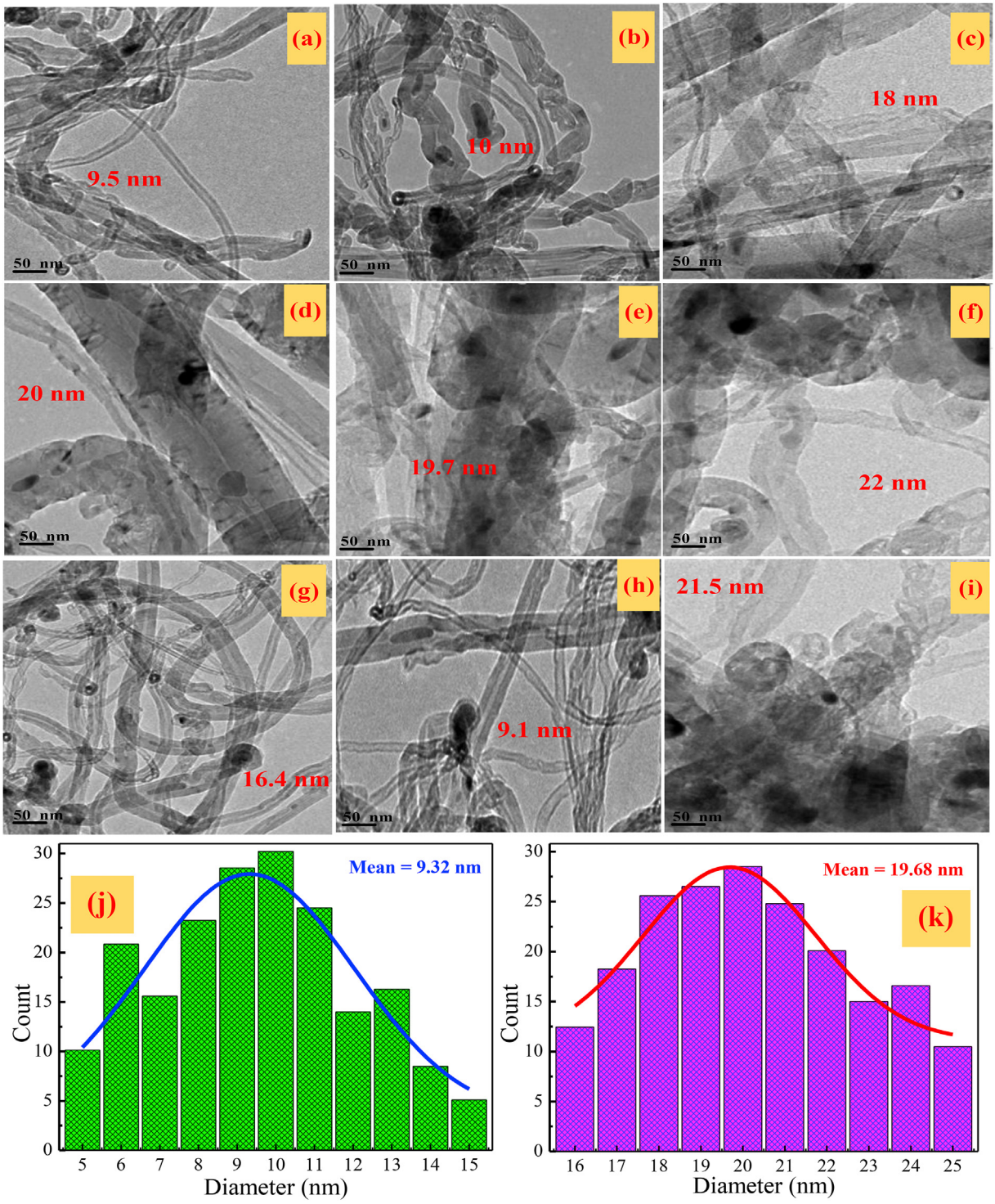

Fig. 1. (a-i) Mean diameter of MWCNTs for the HRTEM analysis of Taguchi L9 OA technique (Runs 1–9); Diameter distribution for (j) **MWCNTs$_{5-15\ nm}$** and (k) **MWCNTs$_{16-25\ nm}$**.

formation of a typical graphite carbon (Jia et al., 2020). The identified peaks on the nanoadsorbents were assigned to the following crystal planes (002), (101) and (102). Overall, XRD patterns identified in this study show crystalline structures of MWCNTs as reported by others (Wu et al., 2020).

The sizes of the crystals for MWCNTs$_{5-15\ nm}$ and MWCNTs$_{16-25\ nm}$ were evaluated using Debyne-Scherrer representation shown in Eq. (26) (Egbosiuba et al., 2020a).

$$D = \frac{k\lambda}{\beta cos\theta} \tag{26}$$

herein, D (nm) and k refers to the crystal size and the shape factor (0.94). Also, β (radians) and λ (nm) represent the full width at half maximum (FWHM) and X-ray wavelength (0.154 nm), while θ (°) is the Bragg's angle. The results indicate that 9.3 and 19.7 nm were

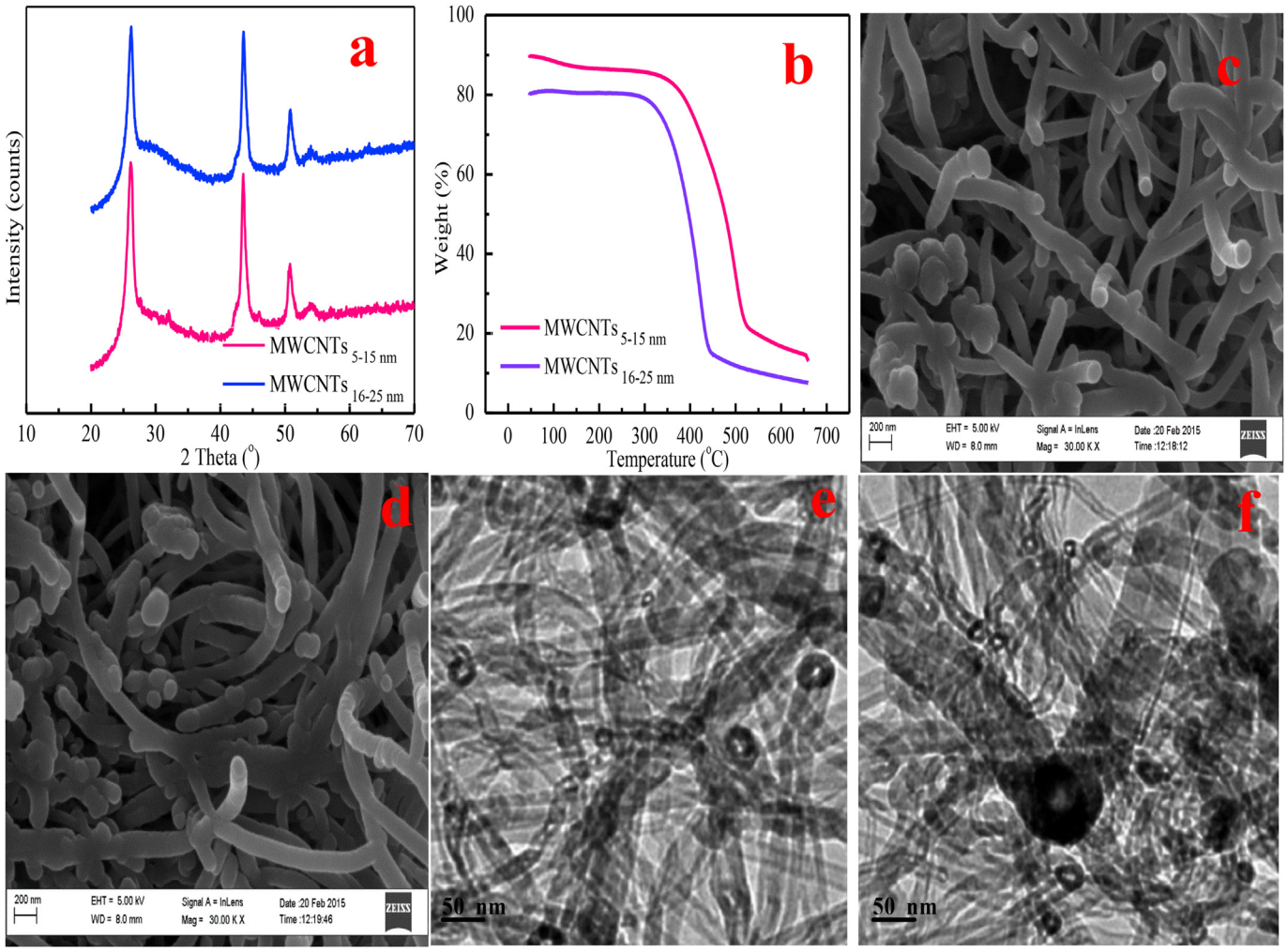

Fig. 2. (a) XRD patterns; (b) TGA; (c) HRSEM of **MWCNTs**$_{5-15\ \mathbf{nm}}$; (d) HRSEM of **MWCNTs**$_{16-25\ \mathbf{nm}}$; (e) HRTEM of **MWCNTs**$_{5-15\ \mathbf{nm}}$ after adsorption of Pb(II) and Ni(II) and (f) HRTEM of **MWCNTs**$_{16-25\ \mathbf{nm}}$ after adsorption of Pb(II) and Ni(II).

obtained as the average crystal sizes for MWCNTs$_{5-15\ nm}$ and MWCNTs$_{16-25\ nm}$, respectively. The smaller crystallite size of MWCNTs$_{5-15\ nm}$ compared to MWCNTs$_{16-25\ nm}$ could be ascribed to the optimized synthesis parameters that narrowed the diameter of the MWCNTs. Notably, the crystallite sizes from the XRD analysis showed strong agreement with the mean diameter of the HRTEM analysis in Fig. 1(j and k).

The TGA profiles of the nanoadsorbents were investigated to evaluate the decomposition of MWCNTs$_{5-15\ nm}$ and MWCNTs$_{16-25\ nm}$ with respect to temperature. Two defined regions of material degradation were observed as shown in Fig. 2(b). For both, the mass decomposition with respect to temperature was gradual between 50 and 360 °C leading to 6.7 wt% and 6.5% weight loss in case of MWCNTs$_{5-15\ nm}$ and MWCNTs$_{16-25\ nm}$, respectively. This could be attributed to the loss of moisture in the nanoadsorbents. Further increase in temperature from 360 to 560 °C resulted in significant weight loss to approx. 64.0 wt% and 63.0 wt% in case of MWCNTs$_{5-15\ nm}$ and MWCNTs$_{16-25\ nm}$, respectively. This could be attributed to the loss of amorphous carbon, decarboxylation and volatilization of the functional groups of MWCNTs. Consistently, it was noticed that beyond the temperatures of 560 and 530 °C, only negligible weight loss occurred on the nanoadsorbents and could be due to the decomposition of residual inorganic and organic moieties. This thermal decomposition profile of MWCNTs was in good agreement with the literature (Jun et al., 2018; Li et al., 2020; Pereira et al., 2019).

Fig. 2(c and d) shows the HRSEM images of the MWCNTs$_{5-15\ nm}$ and MWCNTs$_{16-25\ nm}$ nanoadsorbents. As shown in Fig. 2(c and d), the nanoadsorbents revealed the entangled tubes within the diameter distribution range of 5–15 nm and 16–25 nm. Apparently, the morphological representation of the nanoadsorbents indicate the effectiveness of the purification process due to the observed absence of the metallic impurities and amorphous carbon on the surface. Particularly, the nanoadsorbents illustrated a clear tubular structure of various sizes, which can effectively enhance the diffusion of Pb(II) and Ni(II) ions through the nanoadsorbents. Certainly, the pores specifically provide large surface area and huge number of active sites that favor the uptake of heavy metal ions (Tang et al., 2020). The porous structures of the nanoadsorbents reveals the adsorption routes responsible for possible Ni(II) and Pb(II) ions removal through diffusion to the pores and subsequent attachment to the surface of the nanoadsorbents.

The results of the HRTEM analysis of the nanoadsorbents before and after adsorption studies of Pb(II) and Ni(II) metal ions are shown in Fig. 1(a–i) and Fig. 2(e and f). Accordingly, Fig. 1(a–i) displays the closely contacted network of tubular structures for various mean diameters of the synthesized MWCNTs at the various runs, while Fig. 1(j and k) reveals the diameter counts of the

$MWCNTs_{5-15\ nm}$ and $MWCNTs_{16-25\ nm}$. Also, the tubular and entangled structures of the MWCNTs revealed successful removal of the metallic impurities and amorphous carbon during the purification process. Interestingly, the HRTEM result of the spent nanoadsorbents in Fig. 2(e and f) indicate that the networked aggregates of closely contacted, curved, tangled and tube-like structures of the $MWCNTs_{5-15\ nm}$ and $MWCNTs_{16-25\ nm}$ remained after adsorption experiments (Fig. 1(a–i)). Above all, the identified slight structural variations on the surface of the nanoadsorbents could be ascribed to the attachment of Ni(II) and Pb(II) ions by electrostatic interaction and surface adsorption. The HRTEM results strongly agreed with the XRD and HRSEM analysis shown in Fig. 2(a,c,d). Similar morphological findings have been reported by Maazinejad et al. (2020) after the adsorption of methylene blue (MB) using single walled CNT-NH_2.

In this study, BET analysis was used to further examine the surface properties of the $MWCNTs_{5-15\ nm}$ and $MWCNTs_{16-25\ nm}$. Interestingly, the BET surface area, total pore volume and pore diameter average of $MWCNTs_{5-15\ nm}$ were obtained as $1306 \pm 5\ m^2/g$, $0.91\ cm^3/g$ and 35 nm. Comparatively, notable reduction in the BET surface area ($1245 \pm 4\ m^2/g$), total pore volume ($0.82\ cm^3/g$) and pore diameter average (27 nm) were revealed for the surface properties of $MWCNTs_{16-25\ nm}$. According to the results of the surface properties, both nanoadsorbents were structurally mesoporous as revealed by the average pore diameters of 35 and 27 nm, respectively (Mohamed et al., 2020). The higher surface area observed in $MWCNTs_{5-15\ nm}$ could be attributed to the enhanced influence of synthesis temperature, acetylene flow rate, argon flow rate and synthesis time to produce MWCNTs of smaller diameter. Similarly, it has been reported previously that MWCNTs of smaller diameter possess higher surface area, while MWCNTs of larger diameter has lower surface area (Peigney et al., 2001; Yang et al., 2017; Zhao et al., 2019).

3.3. Adsorption of Pb(II) and Ni(II) by the nanoadsorbents

The investigation of diameter dependent adsorption of Pb(II) and Ni(II) ions has been conducted using the two diameter distribution ranges $MWCNTs_{5-15\ nm}$ and $MWCNTs_{16-25\ nm}$ identified through L_9 OA Taguchi optimization technique. In the adsorption of Pb(II) and Ni(II) ions from chemical industry wastewater, the evaluated process parameters include: pH, contact time, adsorbent dosage and temperature.

3.3.1. Impact of pH

Recent research has suggested that pH of a solution significantly influences the surface properties of nanoadsorbents and chemical species of adsorbate, thereby playing a vital role in the removal of pollutants from wastewater (Qu et al., 2020). As revealed in Fig. 3(a) at constant contact time (20 min), adsorbent dosage (10 mg/L) and temperature (30 °C), the quantity of Pb(II) and Ni(II) ions adsorbed were significantly suppressed in a very acidic condition (pH 2), while a rapid increase in the adsorption of Pb(II) and Ni(II) ions were observed up to pH 5. As expected, more Pb(II) and Ni(II) ions were attached to the surface of $MWCNTs_{5-15\ nm}$ than $MWCNTs_{16-25\ nm}$, which could be ascribed to the smaller diameter and higher surface area of $MWCNTs_{5-15\ nm}$. For Pb(II) and Ni(II) ion adsorption by $MWCNTs_{5-15\ nm}$, the adsorption capacity increased from 98.34 to 110.40 mg/g to 185.20 and 195.60 mg/g respectively in the pH range of 2–5. Whereas, the maximum adsorption capacity increased from 64.20 to 80.81 mg/g to 158.73 and 175.25 mg/g for Pb(II) and Ni(II) ions respectively using $MWCNTs_{16-25\ nm}$. Notably, the observed higher adsorption of Ni(II) ions over Pb(II) ions at the various pH using both nanoadsorbents could be linked to the lower ionic radius of Ni(II) (0.6 Å) (Liu et al., 2020) compared to that of Pb(II) (0.98 Å) (Huang et al., 2020) and higher electronegativity of Ni(II) (1.91) (Liu et al., 2020) than Pb(II) (1.87) (Sellaoui et al., 2019). Therefore, the advantages resulting from lower ionic radius and higher electronegative values of Ni(II) ions over Pb(II) ions induced the enhanced better diffusion of Ni(II) ions into the pores of the adsorption sites on both nanoadsorbents than Pb(II) ions. The pH-dependent metal ions adsorption could be ascribed to the protonation of the active sites of the nanoadsorbents in a high acidic media (Bisheh et al., 2020). Specifically, at a low pH the H^+ ion concentration is high resulting in occupation of functional adsorption sites of MWCNTs by H^+ ions, thus facilitating the competition between Pb(II) and Ni(II) ions adsorption and H^+ ions (Chaabane et al., 2020). It is evident that the protonation of carboxyl and hydroxyl containing functional groups compromised the adsorption ability of the positively charged nanoadsorbent (Bo et al., 2020). Further increase in pH expectedly reduced the competition and as such increased the adsorption of metal ions due to deprotonation of carboxyl and hydroxyl groups that enhanced negative charge on the nanoadsorbents surface (Bo et al., 2020).

Overall, the evaluation of pH_{PZC} enhances the understanding of the underlying adsorption phenomena and Fig. 3(b) shows that pH_{PZC} for the $MWCNTs_{5-15\ nm}$ and $MWCNTs_{16-25\ nm}$ were identified as 6.2 and 6.0, respectively. Based on that, the surface of the nanoadsorbents was positively charged below the pH of 6.2 and 6.0, but negatively charged above the pH of 6.2 and 6.0, respectively. This implies that at $pH < pH_{PZC}$, the positively charged surface of the $MWCNTs_{5-15\ nm}$ and $MWCNTs_{16-25\ nm}$ would unfavorably interact with the positive Pb(II) and Ni(II) ions due to electrostatic repulsion (Oh et al., 2020; Qu et al., 2020). Previously, researchers have reported that polyvalent metal ions could be induced by the carboxyl and hydroxyl groups to precipitate at higher pH ($pH > 6$) (Bo et al., 2020). Sequel to that, maximum adsorption of Pb(II) and Ni(II) ions was achieved at pH 5 and was used for further studies, to avoid the interference due to the precipitation to the hydroxides of Pb(II) ($Pb(OH)_2$) and Ni(II) ($Ni(OH)_2$). The pH (5) reported in this study collaborated with previous studies that reported pH of 5 for Pb(II) and Ni(II) adsorption on MNPs@SiO_2/TSD-TEOS and $CM_{0.5}AP_{0.75}$ (Ahmad et al., 2019; Bo et al., 2020).

3.3.2. Impact of contact time

In order to evaluate the equilibrium time, the influence of contact time on the adsorption capacity of Pb(II) and Ni(II) ions by $MWCNTs_{5-15\ nm}$ and $MWCNTs_{16-25\ nm}$ was investigated at constant pH (5), adsorbent dosage (10 mg/L) and temperature (30 °C) and the result presented in Fig. 3(c). Notably, the quantity of Pb(II) and Ni(II) ions adsorbed increased rapidly over time, until the equilibrium adsorption capacity was achieved after 60 min on both nanoadsorbents. Specifically, the rapid adsorption of metal ions within this period may be due to external diffusion of Pb(II) and Ni(II) ions to the large number of adsorption sites on the nanoadsorbents. In addition, the rapid increase in adsorption could be linked to the increased electrostatic attraction existing among the metal ions and the $MWCNTs_{5-15\ nm}$ and $MWCNTs_{16-25\ nm}$. Unfavorably, further increase in contact time beyond 60 min resulted to the observed negligible adsorption of the metal ions which may be ascribed to the nanoadsorbents active sites saturation and effect of intraparticle diffusion (Kazak et al., 2018). Above all, an increase in the adsorbed amount of Pb(II) and Ni(II) ions by $MWCNTs_{5-15\ nm}$ was observed from 132.55 to 205.57 mg/g and 144.68–216.46 mg/g, whereas the adsorbed amount of Pb(II) and Ni(II) ions onto the $MWCNTs_{16-25\ nm}$ increased from 115.75 to 184.94 mg/g and 123.52–200.84 mg/g, respectively. Comparatively, Ni(II) ions were adsorbed better than Pb(II) ions on both nanoadsorbents and could be linked to the differences in the ionic radius and electronegativity of the metal ions (Chen et al., 2019; Huang et al., 2020; Sellaoui

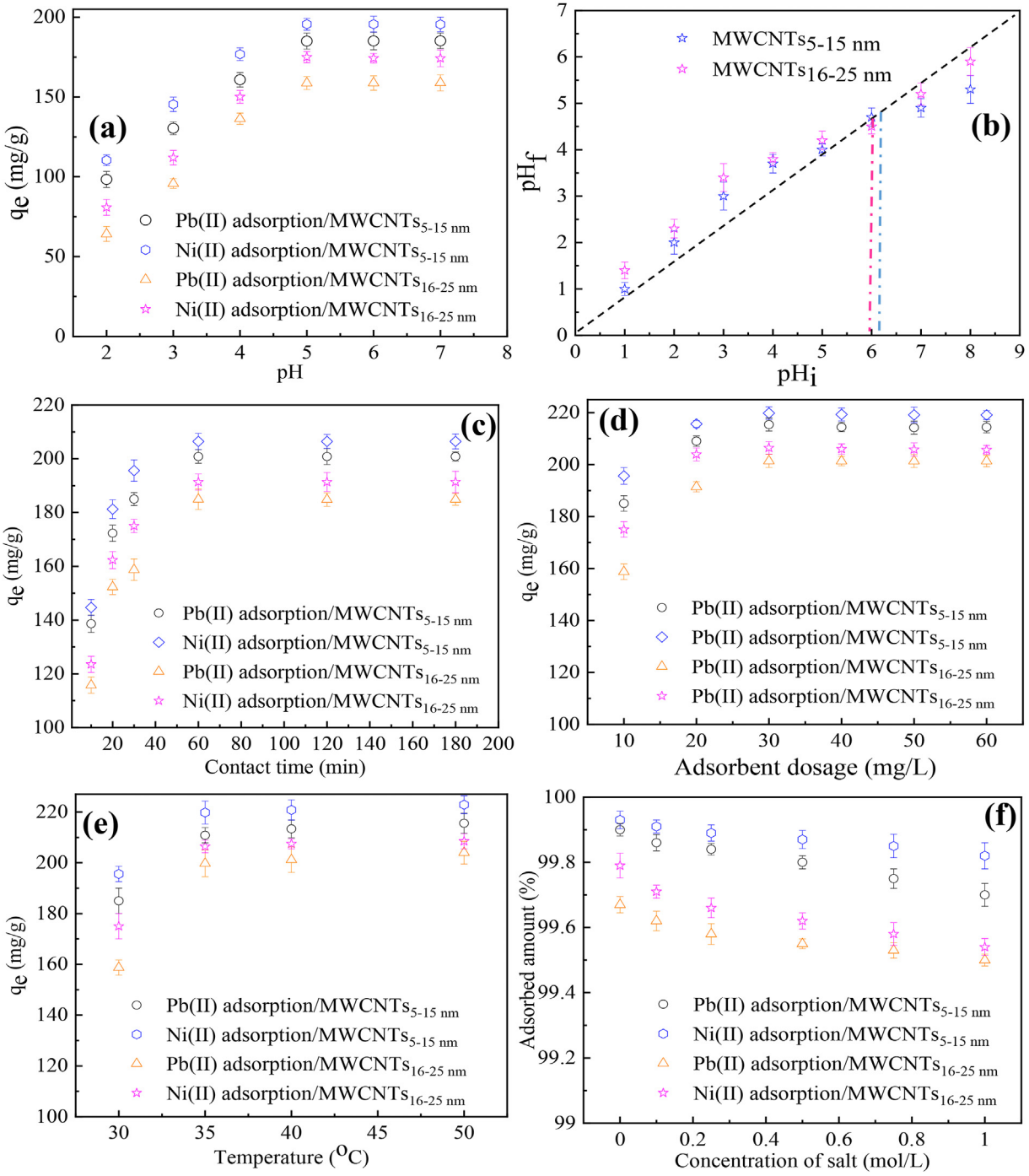

Fig. 3. (a) Impact of pH (at contact time (30 min), adsorbent dosage (10 mg/L) and temperature (30 °C)); (b) Point of zero charge (pHPZC) evaluated by pH drift method; (c) Impact of contact time (at pH (5), adsorbent dosage (10 mg/L) and temperature (30 °C)); (d) adsorbent dosage (at pH (5), contact time (60 min) and temperature (30 °C)); (e) temperature for Pb(II) and Ni(II) adsorption onto **MWCNTs$_{5-15\ nm}$** and **MWCNTs$_{16-25\ nm}$**(at pH (5), contact time (60 min) and adsorbent dosage (30 mg/L)); (f) effect of ionic strength on Pb(II) and Ni(II) adsorption onto **MWCNTs$_{5-15\ nm}$** and **MWCNTs$_{16-25\ nm}$** using 30 mg/L of nano adsorbent at a pH and temperature of 5 and 50 °C for 60 min.

et al., 2019). Over the literature, an equilibrium adsorption time of 60 min was reported for the adsorption of Ni(II) ions using walnut shells biochar adsorbent (WBSA) (Georgieva et al., 2020). Also, Qu et al., (2020) reported an equilibrium adsorption time of 60 min for uptake of Pb(II)/Ni(II) ions from electroplating wastewater using functionalized cellulose.

3.3.3. *Impact of adsorbent dosage*

During adsorption, nanoadsorbent dosage could significantly influence the removal of Pb(II) and Ni(II) ions. As shown in Fig. 3(d) at constant pH (5), contact time (60 min) and temperature (30 °C), fast uptake of the metal ions was revealed as the adsorbent dosage was increased from 10 to 30 mg/L on both MWCNTs$_{5-15\ nm}$ and MWCNTs$_{16-25\ nm}$ which may be attributed to increasing amount of adsorption sites on the nanoadsorbents surface. In this study an increase in adsorption capacity from 185.04 to 215.38 mg/g and from 195.60 to 230.78 mg/g was observed for Pb(II) and Ni(II) ions uptake by MWCNTs$_{5-15\ nm}$, whereas the adsorption of Pb(II) and

Ni(II) ions onto $MWCNTs_{16-25\ nm}$recorded increase in adsorption capacity from 158.73 to 201.35 mg/g and 175.05–206.40 mg/g. Nevertheless, $MWCNTs_{5-15\ nm}$ adsorbed more of the Pb(II) and Ni(II) ions ahead of $MWCNTs_{16-25\ nm}$ which may be due to the higher surface area and stronger electrostatic attraction between the metal ions and the nanoadsorbent. Similarly, the large adsorption capacity observed for Ni(II) ions adsorption on both nanoadsorbent could be due to the differences in ionic radius and electronegativity of the metal ions that effect the uptake efficiency (Kharrazi et al., 2020). Notably, rapid adsorption had been reported for metal ions with lower ionic radius compared to those with higher ionic radius (Huang et al., 2020). Again, metal ions with higher electronegativity adsorbed more easily, than metal ions with lower electronegativity. Compared to Pb(II), Ni(II) had the smaller ionic radius and the greater electronegativity. Similar trend of metal ions adsorption capacity was reported by Sellaoui et al., (2019) in the adsorption of Pb(II), Hg(II) and Zn(II) from aqueous solution on a lignocellulosic biomass char.

3.3.4. Impact of temperature

Temperature is an important adsorption parameter since the temperature increase particularly enhances the diffusion rate of adsorbate molecules in the internal pores and across the external boundary layer of the adsorbent due to decrease in the solution viscosity and mass transfer resistance (Georgieva et al., 2020). Correspondingly, change in temperature also alters the equilibrium capacity of the adsorbent for a specific adsorbate. The impact of temperature on the uptake of Pb(II) and Ni(II) ions by $MWCNTs_{5-15\ nm}$ and $MWCNTs_{16-25\ nm}$ was investigated at a constant pH (5), contact time (60 min) and adsorbent dosage (30 mg/L) and the result presented in Fig. 3(e). Accordingly, Fig. 3(e) revealed a linear increase in the equilibrium adsorption capacity of Pb(II) and Ni(II) ions by $MWCNTs_{5-15\ nm}$and $MWCNTs_{16-25\ nm}$ as a function of temperature. In fact, the adsorption of Ni(II) ions over Pb(II) ions on both nanoadsorbent could be attributed to improved movement of Ni(II) ions to the pores on the nanoadsorbent surface and enhanced binding to the nanoadsorbent surface. The result of this study suggest that the uptake of Pb(II) and Ni(II) ions by $MWCNTs_{5-15\ nm}$ and $MWCNTs_{16-25\ nm}$ was an endothermic process. Above all, it was observed that increase in temperature resulted to an increase in the adsorption capacity of Pb(II) and Ni(II) ions from 185.71 to 229.54 mg/g and from 195.60 to 242.85 mg/g, respectively using $MWCNTs_{5-15\ nm}$. However, the adsorption of Pb(II) and Ni(II) ions by $MWCNTs_{16-25\ nm}$ also increased the adsorption capacity from 158.35 to 206.98 mg/g and from 175.38 to 219.46 mg/g. In another study, Zhao et al., (2020) and Georgieva et al., (2020) also reported an improved adsorption capacity for metal ions uptake with temperature increase.

3.4. Effect of competing ions

The influence of competing ions/ionic strength on the adsorption capacity plays vital role because the solution composition influences the surface charge of $MWCNTs_{5-15\ nm}$ and $MWCNTs_{16-25\ nm}$. On the other hand, the likelihood of competition between the positive ions added (Ca^{2+} and Na^{+}) and the metal ions of interest (Pb(II) and Ni(II)), thus the possible reduction in the diffusion/migration of metal ions to the nanoadsorbents at high ionic strength may accordingly influence the equilibrium adsorption capacity (Zhang et al., 2020). Herein, the effect of competing ions on the adsorption of Pb(II) and Ni(II) ions by the nanoadsorbents was examined and the results are shown in Fig. 3(f). Noticeably in Fig. 3(f), competing ions (Ca^{2+} and Na^{+}) had an insignificant influence on the uptake of Pb(II) and Ni(II) ions at the following optimal adsorption conditions: a constant pH (5), contact time (60 min), adsorbent dosage (30 mg/L) and temperature (50 °C). This observation demonstrated, Pb(II) and Ni(II) ions had a stronger attraction to the surface of the nanoadsorbents compared to Ca(II) and Na. The reason for the strong attraction of the Pb(II) and Ni(II) ions may be attributed to the differences in their ionic radius and electronegative properties. Above all, the ionic radius of Ni(II), Pb(II), Ca(II) and Na are 0.6, 0.98, 1.34 and 1.0 Å (Huang et al., 2020), whereas the electronegativity of Ni(II), Pb(II), Ca(II) and Na are 1.91, 1.87, 1.0 and 0.93, respectively (Sellaoui et al., 2019). Hence, Pb(II) and Ni(II) ions with smaller ionic radius and higher electronegativity were adsorbed better on the nanoadsorbents surface due to stronger electrostatic interactions between the nanoadsorbents and the metal ions, than the competing ions.

3.5. Isotherm modelling

In view of exploring the interactive behaviors between the Pb(II)/Ni(II) ions and the nanoadsorbents at the optimal conditions of pH (5), contact time (60 min), adsorbent dosage (30 mg/L) and temperature (50 °C), the adsorption isotherms of $MWCNTs_{5-15\ nm}$ and $MWCNTs_{16-25\ nm}$ were examined. To describe the adsorption process, the initial concentration (C_o) of Pb(II) and Ni(II) ions in the chemical industrial wastewater were identified as 62 and 66 mg/L, respectively. On the completion of the wastewater treatment, the concentration at equilibrium (C_e) of 0.06 and 0.04 mg/L were achieved for Pb(II) and Ni(II) ions using $MWCNTs_{5-15\ nm}$. Whereas, the C_e for Pb(II) and Ni(II) were obtained as 0.09 and 0.05 mg/L, respectively using $MWCNTs_{16-25\ nm}$. Additionally, the obtained C_e using further validates the better adsorption of the metal ions by $MWCNTs_{5-15\ nm}$ than $MWCNTs_{16-25\ nm}$ due to smaller diameter impact. However, the concentrations of Pb(II) and Ni(II) ions after treatment by both nanoadsorbents significantly fall within the permissible standard concentration of 0.1 mg/L for Pb(II) and Ni(II) ions proposed by WHO and US, EPA (US EPA, 2012; WHO, 2017).

To establish the interaction between Pb(II)/Ni(II) ions and the nanoadsorbents, adsorption isotherms was used by fitting the experimental data to the Langmuir, Freundlich, Temkin and Dubinin-Radushkevich model and thereafter comparing the obtained equilibrium adsorption data. According to Fig. 4(a,b), S2, S3, S4 and the calculated adsorption parameters enumerated in Table 2, Langmuir isotherm model suitably described the adsorption of Pb(II) and Ni(II) ions by $MWCNTs_{5-15\ nm}$ and $MWCNTs_{16-25\ nm}$, respectively due to the larger values of coefficient of determination (R^2) and lower error values of SSE and X^2 (Eq. (S1) and (S2)). Hence, this result implies that the adsorption of Pb(II) and Ni(II) ions occurred primarily by chemisorption controlled monolayer coverage of the homogeneous surface of the nanoadsorbents (Qu et al., 2020).

In this study, the maximum adsorption capacity (q_m) (Table 2) was realized for Pb(II) (215.38 mg/g) and Ni(II) (230.78 mg/g) using $MWCNTs_{5-15\ nm}$, while metal ions adsorption using $MWCNTs_{16-25\ nm}$ were obtained as Pb(II) (201.35 mg/g) and Ni(II) (206.40 mg/g). Again, the Langmuir isotherm parameter, R_L (fall between 0 and 1) and Freundlich adsorption intensity, n_F (greater than 1) demonstrates outstanding Pb (II) and Ni(II) ions adsorption by nanoadsorbents of varied diameter distribution ($MWCNTs_{5-15\ nm}$ and $MWCNTs_{16-25\ nm}$).

On the other hand, the investigated adsorption conditions and adsorption capacities in the present study were compared with the previous studies over the literature as presented in Table 3. In all, the adsorption capacities of the nanoadsorbents in this study were relatively higher than most others, except for the adsorption capacities of 295.0 and 414.4 mg/g reported for Pb(II) and Ni(II) ions using RH_{MW}-X and Na-SGS (Qu et al., 2020; Su et al., 2020). The adsorption capacities reported by the researchers could be due to

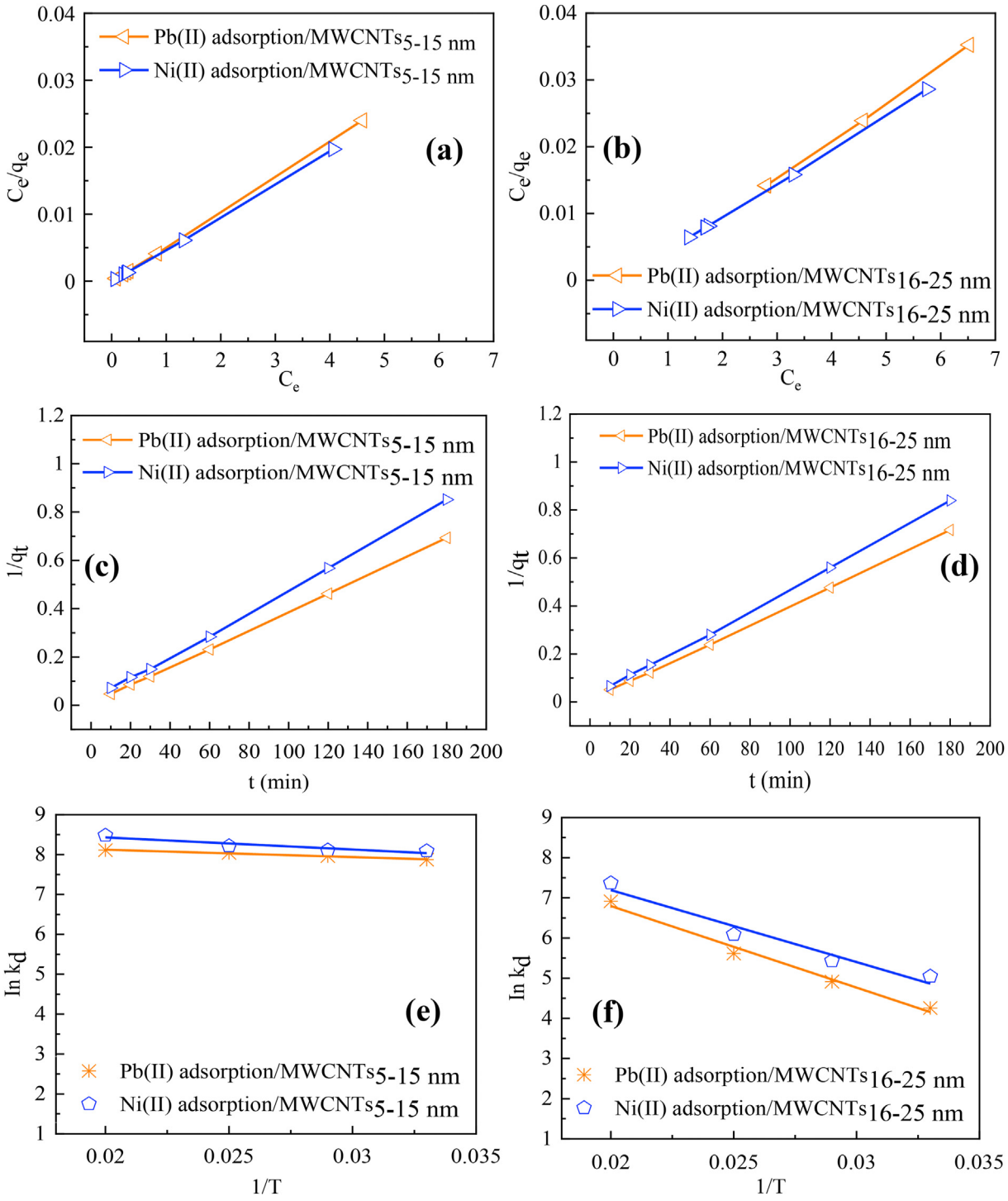

Fig. 4. (a) Langmuir isotherm model of Pb(II) and Ni(II) adsorption onto **MWCNTs**$_{5-15\ nm}$; (b) Langmuir isotherm model of Pb(II) and Ni(II) adsorption onto **MWCNTs**$_{16-25\ nm}$ using pH (5), contact time (60 min) and temperature (30 °C). (c) pseudo-second order kinetics of Pb(II) and Ni(II) adsorption onto **MWCNTs**$_{5-15\ nm}$; (d) pseudo-second order kinetics of Pb(II) and Ni(II) adsorption onto **MWCNTs**$_{16-25\ nm}$; at pH (5), adsorbent dosage (30 mg/L) and temperature (30 °C) (e) Thermodynamics of Pb(II) and Ni(II) adsorption onto **MWCNTs**$_{5-15\ nm}$; (f) Thermodynamics of Pb(II) and Ni(II) adsorption onto **MWCNTs**$_{16-25\ nm}$ at pH (5), contact time (60 min) and adsorbent dosage (30 mg/L).

the simulated wastewater used, against the real wastewater in this study which encompasses different competing scavengers including nitrates, phosphates, chlorides, carbonates and sulphates.

3.6. Kinetic modelling

Adsorption kinetics is an efficient time-dependent technique for evaluating the removal rates of Pb(II) and Ni(II) ions by the nano-adsorbents. Therefore, the experimental data were fitted into pseudo-first-order, pseudo-second- order, Elovich and intra-particle diffusion model, respectively. As shown by the fitted curves and calculated parameters in Fig. 4(c,d), S5 and Table 4, the pseudo-second order model fit the experimental data better than the pseudo-first order, Elovich and intraparticle diffusion model

Table 2
Evaluated parameters of an isotherm model for uptake of Pb(II) and Ni(II) by **MWCNTs$_{5-15\ nm}$** and **MWCNTs$_{16-25\ nm}$**.

Isotherm model	Parameters	**MWCNTs$_{5-15\ nm}$**		**MWCNTs$_{16-25\ nm}$**	
		Pb(II)	Ni(II)	Pb(II)	Ni(II)
Langmuir	q_m(mg/g)	215.38 ± 0.03	230.78 ± 0.01	201.35 ± 0.02	206.40 ± 0.02
	K_L (L.min^{-1})	0.05 ± 0.02	0.03 ± 0.02	0.05 ± 0.02	0.04 ± 0.01
	R_L	0.44 ± 0.01	0.56 ± 0.01	0.31 ± 0.02	0.52 ± 0.01
	R^2	0.999	0.999	0.999	0.999
	SSE	0.03	0.12	0.04	0.04
	X^2	0.01	0.01	0.08	0.08
Freundlich	n_F	2.30 ± 0.08	2.32 ± 0.08	2.33 ± 0.08	2.34 ± 0.08
	K_F (mg/g)	199.75 ± 0.07	213.74 ± 0.09	213.01 ± 0.07	219.84 ± 0.09
	R^2	0.816	0.805	0.990	0.971
	SSE	1.64	1.37	0.05	0.49
	X^2	0.05	0.03	0.10	0.15
Temkin	B (kJ/mol)	199.87 ± 0.03	213.82 ± 0.01	211.99 ± 0.03	219.62 ± 0.02
	K_t (L/mg)	0.98 ± 0.03	0.99 ± 0.05	0.94 ± 0.03	0.96 ± 0.02
	R^2	0.819	0.809	0.991	0.973
	SSE	1.56	1.32	3.25	6.93
	X^2	0.05	0.03	0.21	4.84
D-R	K_{DR}	1.0×10^{-7} ± 0.02	0.1×10^{-7} ± 0.01	2.0×10^{-7} ± 0.02	5.0×10^{-7} ± 0.01
	q_m	199.46 ± 0.02	213.41 ± 0.01	183.55 ± 0.02	202.67 ± 0.02
	R^2	0.834	0.838	0.944	0.838
	SSE	3.47	3.18	6.90	6.35
	X^2	0.24	0.19	1.04	0.80

Table 3
Comparison of adsorption parameters, maximum adsorption capacity, isotherm and kinetic model for Pb(II) and Ni(II) adsorption by **MWCNTs$_{5-15\ nm}$** and **MWCNTs$_{16-25\ nm}$** with different designated adsorbents over the literature.

Adsorbent	Adsorption parameters					Adsorption capacity (mg/g)		Isotherm/Kinetic model	Reference
	C_o (mg/L)	pH (Pb/Ni)	Time (min)	Dosage (mg)	Temp. (°C)	Pb(II)	Ni(II)		
CNT-TRI	5	6	180	30	25	15.9	–	Freundlich/IPD[a]	(Albakri et al., 2018)
MGO	60	5/8	30	16	45	200.0	51.0	Langmuir/PSO[b]	Ain et al. (2020)
POP-NH_2	30	7	–	15	25	37.8	33.2	Langmuir/PSO	Bisheh et al. (2020)
MWNPs	5	6	120	100	25	–	32.2	Langmuir/PSO	(Dehghani et al., 2019)
Co−Fe_2O_4	100	7	45	25	25	136.0	–	Freundlich/PFO[c]	Chen et al. (2019)
Fe_3O_4@TiO_2−CN	100	5.5	60	60	25	92.6	75.8	Langmuir/PSO	(Mousavi et al., 2019)
CTS/SA/Ca^{2+}PCDNH	20	–	480	25	25	176.0	–	Freundlich/PFO	Tang et al. (2020)
RH_{MW}-X	2/2	5.5	30	100	20	295.0	72.8	Langmuir/PSO	Qu et al. (2020)
WSBA	50	6.5	60	3	30	–	13.9	Langmuir/PSO	Georgieva et al. (2020)
SLFP	100	5	720	200	25	39.5	–	Langmuir/PSO	Zhang et al. (2020)
Na-SGS	500	5	1440	30	40	–	414.4	Langmuir/PSO	Su et al. (2020)
MLTA-P	500	6		30	28	–	100.0	Langmuir/PSO	(Hong et al., 2019)
$MWCNTs_{5-15\ nm}$	62/66	5.8	60	30	50	215.38	230.78	Langmuir/PSO	This study
$MWCNTs_{16-25\ nm}$	62/66	6	60	30	50	201.35	206.40	Langmuir/PSO	This study

NB: a = Intraparticle diffusion; b = Pseudo-second order and c = Pseudo-first order.

due to the observed high values of R^2 and low values of the SSE and X^2. Also, the value of calculated adsorption capacity ($q_{e,\ cal}$) using pseudo-second order model for $MWCNTs_{5-15\ nm}$ (Pb(II) (196.08 mg/g) and Ni(II) (212.77 mg/g)) and $MWCNTs_{16-25\ nm}$ (Pb(II) (188.68 mg/g) and Ni(II) (204.08 mg/g)) closely correlated with the experimental adsorption capacity ($q_{e,\ exp}$) for $MWCNTs_{5-15\ nm}$ (Pb(II) (205.57 mg/g) and Ni(II) (216.46 mg/g)) and $MWCNTs_{16-25\ nm}$ (Pb(II) (184.94 mg/g) and Ni(II) (200.84 mg/g)). Above all, the matching fitness with the pseudo-second-order kinetic model is an indication that the adsorption of Pb(II) and Ni(II) ions onto the nanoadsorbents were principally chemisorption controlled, suggesting the formation of chemical bonds in the adsorption process through sharing, relocation and transfer of electrons (Ain et al., 2020).

3.7. Thermodynamics

The results of the thermodynamic parameters determination are presented in Fig. 4(e and f), while the calculated parameters are shown in Table 5.

As shown in Table 5, the positive ΔH° values revealed that the uptake of Pb(II) and Ni(II) ions by both nanoadsorbents were endothermic and chemisorption in nature. The values of ΔH° shows correspondence whether the adsorption process is physisorption or chemisorption controlled. Meanwhile, the magnitude of ΔH° < 40 kJ/mol defines physisorption, while ΔH° > 40 kJ/mol is an indication of chemisorption controlled adsorption process (Cheng et al., 2017). Herein, the obtained negative values of ΔG° indicate a feasible and spontaneous adsorption process with sufficient adsorptive forces to overpower any potential barrier (Ain et al., 2020). Again, the decrease in the ΔG° values observed with temperature increase demonstrates the favorability of the adsorption of Pb(II) and Ni(II) at elevated temperatures (Maazinejad et al., 2020). In addition, the sign and degree of ΔS° describe whether the arrangement of Pb(II) and Ni(II) at solid-liquid phase was more likely ($\Delta S^\circ > 0$) or less random ($\Delta S^\circ < 0$) (Qu et al., 2020). In this study, the positive ΔS° values indicate nanoadsorbent affinity and increasing randomness at the solid-liquid interface during the

Table 4
Evaluated parameters of kinetic model for uptake of Pb(II) and Ni(II) by **MWCNTs$_{5-15\ nm}$** and **MWCNTs$_{16-25\ nm}$**.

Kinetic model	Parameters	**MWCNTs$_{5-15\ nm}$**		**MWCNTs$_{16-25\ nm}$**	
		Pb(II)	Ni(II)	Pb(II)	Ni(II)
Pseudo-first order	$q_{e,exp}$(mg/g)	205.57 ± 0.02	216.46 ± 0.01	184.94 ± 0.01	200.84 ± 0.02
	$q_{e,cal}$(mg/g)	233.02 ± 0.01	199.25 ± 0.01	270.89 ± 0.01	221.62 ± 0.01
	K_1 (g mg^{-1} min^{-1})	−0.11 ± 0.01	−0.11 ± 0.02	−0.12 ± 0.03	−0.12 ± 0.05
	R^2	0.977	0.989	0.954	0.989
	SSE	7.61	1.32	15.71	3.79
	X^2	7.45	0.26	27.34	1.95
Pseudo-second order	$q_{e,cal}$(mg/g)	196.08 ± 0.03	212.77 ± 0.03	188.68 ± 0.02	204.08 ± 0.02
	K_2 (g mg^{-1} min^{-1})	0.001 ± 0.035	0.002 ± 0.032	0.001 ± 0.027	0.002 ± 0.028
	R^2	0.999	1.000	0.999	1.000
	SSE	0.86	1.15	0.70	0.59
	X^2	0.11	0.19	0.08	0.05
Elovich	α (g mg^{-1} min^{-2})	816.75 ± 0.04	2700.81 ± 0.03	500.11 ± 0.04	2314.94 ± 0.03
	β (mg g^{-1} min^{-1})	0.04 ± 0.01	0.04 ± 0.01	0.04 ± 0.01	0.04 ± 0.01
	R^2	0.860	0.854	0.867	0.836
	SSE	114.18	455.40	57.56	385.98
	X^2	478.88	2302.67	198.76	1930.69
Intraparticle diffusion	K_3(g mg^{-1} min^{-1})	5.03 ± 0.02	4.59 ± 0.03	5.25 ± 0.05	4.50 ± 0.02
	C (mg/g)	136.29 ± 0.02	156.21 ± 0.01	227.32 ± 0.01	184.98 ± 0.01
	R^2	0.549	0.545	0.553	0.524
	SSE	10.05	9.17	10.50	14.55
	X^2	22.25	16.17	8.98	13.08

Table 5
Thermodynamic parameters for adsorption of Pb(II) and Ni(II) by **MWCNTs$_{5-15\ nm}$** and **MWCNTs$_{16-25\ nm}$**.

Heavy metal	T (°C)	**MWCNTs$_{5-15\ nm}$**			**MWCNTs$_{16-25\ nm}$**		
		ΔG° (kJ/mol)	ΔH° (kJ/mol)	ΔS° (J/mol)	ΔG° (kJ/mol)	ΔH° (kJ/mol)	ΔS° (kJ/mol)
Pb(II)	30	−1964.50 ± 0.01	151.68 ± 0.01	70.54 ± 0.02	−1024.37 ± 0.07	1658.64 ± 0.06	89.43 ± 0.05
	35	−2669.89 ± 0.02			−1918.70 ± 0.01		
	40	−3375.28 ± 0.02			−2813.04 ± 0.02		
	50	−4080.68 ± 0.03			−3707.38 ± 0.01		
Ni(II)	30	−2002.87 ± 0.02	245.28 ± 0.01	74.94 ± 0.02	−1203.37 ± 0.03	1457.94 ± 0.08	88.71 ± 0.07
	35	−2752.25 ± 0.04			−2090.47 ± 0.02		
	40	−3501.63 ± 0.01			−2977.58 ± 0.04		
	50	−4251.01 ± 0.03			−3864.68 ± 0.02		

adsorption of Pb(II) and Ni(II) ions. Furthermore, the negative ΔG° showed that the adsorption of Pb(II) and Ni(II) ions by MWCNTs$_{5-15\ nm}$ and MWCNTs$_{16-25\ nm}$ favorably and spontaneously occurred with a corresponding minimal conditions of adsorption and energies.

3.8. Desorption and reusability evaluation

In view of ensuring cost minimization at the industrial level and prevention of solid waste pollution during adsorption process, the renewability of MWCNTs$_{5-15\ nm}$ and MWCNTs$_{16-25\ nm}$ was investigated. As revealed in Fig. 5(a and b), the uptake efficiencies of Pb(II) and Ni(II) by MWCNTs$_{5-15\ nm}$ and MWCNTs$_{16-25\ nm}$ were almost 100% in the 1st and 2nd cycles. However, further renewability assessment up to the 6th cycle revealed a reduction in the adsorption efficiency to Pb(II) (95%) and Ni(II) (97%) by MWCNTs$_{5-15\ nm}$. Similarly, the removal efficiencies after 6th cycle using MWCNTs$_{16-25\ nm}$ were observed to be Pb(II) (95%) and Ni(II) (96%).

The observed small reduction in the adsorption performance could be ascribed to the unreleased Pb(II) and Ni(II) ions attached on the nanoadsorbent, thereby occupying some adsorption sites as shown by EDX results in Table S4. Notably, Fig. 5(c and d) demonstrated the HRSEM of the nanoadsorbents after 6th cycle, indicating morphological modification and the attached metal ions on the nanoadsorbents adsorptive sites. However, the tube-like structures of the nanoadsorbents can be clearly seen after 6th cycle (Fig. 5(c and d)). In view of cost minimization and protection of the environment, the MWCNTs$_{5-15\ nm}$ and MWCNTs$_{16-25\ nm}$ has reliably been confirmed as an excellent reusable nanoadsorbent for heavy metals removal from wastewater.

4. Conclusion

The MWCNTs$_{5-15\ nm}$ and MWCNTs$_{16-25\ nm}$ were successfully prepared by L_9 (3^4) orthogonal array technique for uptake of Pb(II) and Ni(II) ions. The optimum parameters for synthesis of MWCNTs controlled diameter were: temperature (800 °C), acetylene flow rate (200 mL/min), argon flow rate (100 mL/min) and time (60 min). The XRD, TGA, HRSEM and HRTEM techniques revealed the crystalline nature, thermal profile, entangled tubes, contacted network and tubular structures of MWCNTs. Accordingly, smaller diameter MWCNTs$_{5-15\ nm}$ showed better surface area of 1306 ± 5 m^2/g than larger diameter MWCNTs$_{16-25\ nm}$ (1245 ± 4 m^2/g). From the adsorption studies, both nanoadsorbents exhibited excellent removal of the Pb(II) and Ni(II) ions from

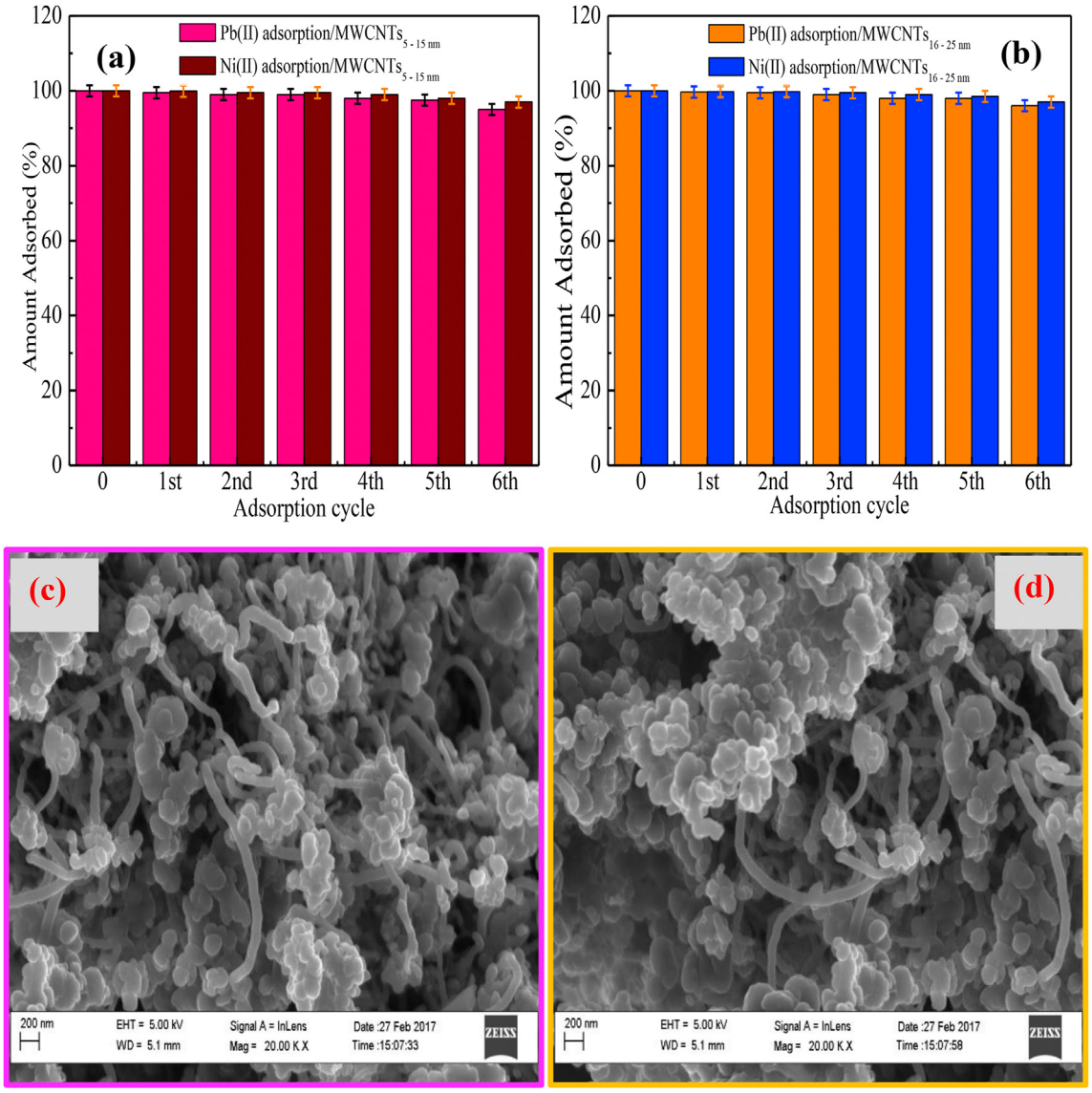

Fig. 5. Reusability evaluation of (a) **MWCNTs$_{5-15\ nm}$** (b) **MWCNTs$_{16-25\ nm}$** for Pb(II) and Ni(II) adsorption; HRSEM image of regenerated (c) **MWCNTs$_{5-15\ nm}$** and (d) **MWCNTs$_{16-25\ nm}$** after the 6th cycle.

industrial wastewater at the pH (5), contact time (60 min), adsorbent dosage (30 mg/L) and temperature (50 °C). Specifically, the obtained maximum adsorption capacity were higher for Pb(II) (215.38 mg/g) and Ni(II) (230.78 mg/g) adsorption using MWCNTs$_{5-15\ nm}$, compared to 201.35 and 206.40 mg/g achieved for Pb(II) and Ni(II) ions by MWCNTs$_{16-25\ nm}$. The experimental data fitted the Langmuir isotherm and pseudo-second order kinetic model, while the thermodynamic evaluation confirmed the endothermic, favorable, spontaneous and chemisorption controlled adsorption process. In view of cost minimization and protection of the environment, the MWCNTs$_{5-15\ nm}$ and MWCNTs$_{16-25\ nm}$ showed reliability as an excellent reusable nanoadsorbent for heavy metals removal from wastewater.

Conflicting interests declaration

The author(s) declared no potential conflicts of interest.

Declaration of competing interest

The authors declare that they have no known competing financial interests or personal relationships that could have appeared to influence the work reported in this paper.

Acknowledgements

This research was made possible through the financial support of the Petroleum Technology Development Fund, Nigeria (grant number PTDF/ED/LSS/PhD/TCE/123/17). SCARCE is supported by the National Research Foundation, Prime Minister's Office, Singapore, the Ministry of National Development, Singapore, and National Environment Agency, Ministry of Sustainability and the Environment, Singapore under the Closing the Waste Loop R&D Initiative as part of the Urban Solutions & Sustainability – Integration Fund (Award No. USS-IF-2018-4).

Appendix A. Supplementary data

Supplementary data to this article can be found online at https://doi.org/10.1016/j.chemosphere.2020.128937.

References

Ahmad, N., Sereshti, H., Mousazadeh, M., Rashidi Nodeh, H., Kamboh, M.A., Mohamad, S., 2019. New magnetic silica-based hybrid organic-inorganic nanocomposite for the removal of lead(II) and nickel(II) ions from aqueous solutions. Mater. Chem. Phys. 226, 73–81. https://doi.org/10.1016/j.matchemphys.2019.01.002.

Ain, Q.U., Farooq, M.U., Jalees, M.I., 2020. Application of magnetic graphene oxide for water purification: heavy metals removal and disinfection. J. Water Process Eng. 33, 101044. https://doi.org/10.1016/j.jwpe.2019.101044.

Albakri, M.A., Abdelnaby, M.M., Saleh, T.A., Al Hamouz, O.C.S., 2018. New series of benzene-1,3,5-triamine based cross-linked polyamines and polyamine/CNT composites for lead ion removal from aqueous solutions. Chem. Eng. J. 333, 76–84. https://doi.org/10.1016/j.cej.2017.09.152.

Bankole, M.T., Mohammed, I.A., Abdulkareem, A.S., Tijani, J.O., Ochigbo, S.S., Abubakre, O.K., Afolabi, A.S., 2018. Optimization of supported bimetallic (Fe-Co/CaCO3) catalyst synthesis parameters for carbon nanotubes growth using factorial experimental design. J. Alloys Compd. https://doi.org/10.1016/j.jallcom.2018.03.150.

Bisheh, M.G., Ghorbani, M., Peyravi, M., Jahanshahi, M., 2020. Static and dynamic filtration of nickel and lead ions by adsorptive membrane induced by POP via layer by layer technique. Chem. Eng. Res. Des. 153, 829–838. https://doi.org/10.1016/j.cherd.2019.11.033.

Bo, S., Luo, J., An, Q., Xiao, Z., Wang, H., Cai, W., Zhai, S., Li, Z., 2020. Efficiently selective adsorption of Pb(II) with functionalized alginate-based adsorbent in batch/column systems: mechanism and application simulation. J. Clean. Prod. 250, 119585. https://doi.org/10.1016/j.jclepro.2019.119585.

Bora, A.J., Dutta, R.K., 2019. Removal of metals (Pb, Cd, Cu, Cr, Ni, and Co)from drinking water by oxidation-coagulation-absorption at optimized pH. J. Water Process Eng. 31, 100839. https://doi.org/10.1016/j.jwpe.2019.100839.

Chaabane, L., Beyou, E., El Ghali, A., Baouab, M.H.V., 2020. Comparative studies on the adsorption of metal ions from aqueous solutions using various functionalized graphene oxide sheets as supported adsorbents. J. Hazard Mater. 389, 121839. https://doi.org/10.1016/j.jhazmat.2019.121839.

Chen, Q., Zheng, J., Wen, L., Yang, C., Zhang, L., 2019. A multi-functional-group modified cellulose for enhanced heavy metal cadmium adsorption: performance and quantum chemical mechanism. Chemosphere 224, 509–518. https://doi.org/10.1016/j.chemosphere.2019.02.138.

Chen, W.Q., Veksha, A., Lisak, G., 2020. Graphene-like Carbon Nanosheets Grown over Alkali-Earth Metal Oxides: Effects of Chemical Composition and Physico-Chemical Properties, Carbon. Elsevier Ltd. https://doi.org/10.1016/j.carbon.2019.12.048.

Cheng, S., Zhang, L., Xia, H., Peng, J., Shu, J., Li, C., Jiang, X., Zhang, Q., 2017. Adsorption behavior of methylene blue onto waste-derived adsorbent and exhaust gases recycling. RSC Adv. 7, 27331–27341. https://doi.org/10.1039/c7ra01482a.

Das, D., Roy, A., 2020. Synthesis of diameter controlled multiwall carbon nanotubes by microwave plasma-CVD on low-temperature and chemically processed Fe nanoparticle catalysts. Appl. Surf. Sci. 515, 146043. https://doi.org/10.1016/j.apsusc.2020.146043.

Dehghani, M.H., Sarmadi, M., Alipour, M.R., Sanaei, D., Abdolmaleki, H., Agarwal, S., Gupta, V.K., 2019. Investigating the equilibrium and adsorption kinetics for the removal of Ni (II) ions from aqueous solutions using adsorbents prepared from the modified waste newspapers: A low-cost and available adsorbent. Microchem. J. 146, 1043–1053. https://doi.org/10.1016/j.microc.2019.02.042.

Egbosiuba, T.C., Abdulkareem, A.S., Kovo, A.S., Afolabi, E.A., Tijani, J.O., Auta, M., Roos, W.D., 2020. Ultrasonic enhanced adsorption of methylene blue onto the optimized surface area of activated carbon: adsorption isotherm, kinetics and thermodynamics. Chem. Eng. Res. Des. https://doi.org/10.1016/j.cherd.2019.10.016.

Egbosiuba, T.C., Abdulkareem, A.S., Kovo, A.S., Afolabi, E.A., Tijani, J.O., Roos, W.D., 2020. Enhanced adsorption of as (V) and Mn (VII) from industrial wastewater using multi-walled carbon nanotubes and carboxylated multi-walled carbon nanotubes. Chemosphere 254, 126780. https://doi.org/10.1016/j.chemosphere.2020.126780.

Georgieva, V.G., Gonsalvesh, L., Tavlieva, M.P., 2020. Thermodynamics and kinetics of the removal of nickel (II) ions from aqueous solutions by biochar adsorbent made from agro-waste walnut shells. J. Mol. Liq. 112788 https://doi.org/10.1016/j.molliq.2020.112788.

Ghosh, S.B., Mondal, N.K., 2019. Application of Taguchi method for optimizing the process parameters for the removal of fluoride by Al-impregnated Eucalyptus bark ash. Environ. Nanotechnology, Monit. Manag. 11 https://doi.org/10.1016/j.enmm.2018.100206.

Govarthanan, M., Lee, K.J., Cho, M., Kim, J.S., Kamala-Kannan, S., Oh, B.T., 2013. Significance of autochthonous Bacillus sp. KK1 on biomineralization of lead in mine tailings. Chemosphere 90, 2267–2272. https://doi.org/10.1016/j.chemosphere.2012.10.038.

Govarthanan, M., Mythili, R., Selvankumar, T., Kamala-Kannan, S., Kim, H., 2018. Myco-phytoremediation of arsenic- and lead-contaminated soils by Helianthus annuus and wood rot fungi, Trichoderma sp. isolated from decayed wood. Ecotoxicol. Environ. Saf. 151, 279–284. https://doi.org/10.1016/j.ecoenv.2018.01.020.

Ho, Y.S., 2006. Second-order kinetic model for the sorption of cadmium onto tree fern: a comparison of linear and non-linear methods. Water Res. 40, 119–125. https://doi.org/10.1016/j.watres.2005.10.040.

Hong, M., Yu, L., Wang, Y., Zhang, J., Chen, Z., Dong, L., Zan, Q., Li, R., 2019. Heavy metal adsorption with zeolites: The role of hierarchical pore architecture, Chemical Engineering Journal. Elsevier B.V. https://doi.org/10.1016/j.cej.2018.11.087.

Huang, X., Zemlyanov, D.Y., Diaz-Amaya, S., Salehi, M., Stanciu, L., Whelton, A.J., 2020. Competitive heavy metal adsorption onto new and aged polyethylene under various drinking water conditions. J. Hazard Mater. 385, 121585. https://doi.org/10.1016/j.jhazmat.2019.121585.

Idris, F.N., Nadzir, M.M., Abd Shukor, S.R., 2020. Optimization of solvent-free microwave extraction of Centella asiatica using Taguchi method. J. Environ. Chem. Eng., 103766 https://doi.org/10.1016/j.jece.2020.103766.

Jia, J., Veksha, A., Lim, T.T., Lisak, G., 2020. In situ grown metallic nickel from X–Ni (X=La, Mg, Sr) oxides for converting plastics into carbon nanotubes: influence of metal–support interaction. J. Clean. Prod. 258 https://doi.org/10.1016/j.jclepro.2020.120633.

Jun, L.Y., Mubarak, N.M., Yon, L.S., Bing, C.H., Khalid, M., Abdullah, E.C., 2018. Comparative study of acid functionization of carbon nanotube via ultrasonic and reflux mechanism. J. Environ. Chem. Eng. 6, 5889–5896. https://doi.org/10.1016/j.jece.2018.09.008.

Kadir Yesilyurt, M., Cesur, C., 2020. Biodiesel synthesis from Styrax officinalis L. seed oil as a novel and potential non-edible feedstock: a parametric optimization study through the Taguchi technique. Fuel 265, 117025. https://doi.org/10.1016/j.fuel.2020.117025.

Kazak, O., Eker, Y.R., Bingol, H., Tor, A., 2018. Preparation of chemically-activated high surface area carbon from waste vinasse and its efficiency as adsorbent material. J. Mol. Liq. 272, 189–197. https://doi.org/10.1016/j.molliq.2018.09.085.

Kharrazi, S.M., Mirghaffari, N., Dastgerdi, M.M., Soleimani, M., 2020. A Novel Post-modification of Powdered Activated Carbon Prepared from Lignocellulosic Waste through Thermal Tension Treatment to Enhance the Porosity and Heavy Metals Adsorption. Powder Technology. Elsevier B.V. https://doi.org/10.1016/j.powtec.2020.01.065.

Langmuir, I., 1918. The adsorption of gases on plane surfaces of glass, mica and platinum. J. Am. Chem. Soc. 40, 1361–1403. https://doi.org/10.1021/ja02242a004.

Li, Y.J., Ma, C., Kang, J.L., Shi, J.L., Shi, Q., Wu, D.H., 2017. Preparation of diameter-controlled multi-wall carbon nanotubes by an improved floating-catalyst chemical vapor deposition method. Xinxing Tan Cailiao/New Carbon Mater 32, 234–241. https://doi.org/10.1016/S1872-5805(17)60120-3.

Li, Z., Sellaoui, L., Franco, D., Netto, M.S., Georgin, J., Dotto, G.L., Bajahzar, A., Belmabrouk, H., Bonilla-Petriciolet, A., Li, Q., 2020. Adsorption of hazardous dyes on functionalized multiwalled carbon nanotubes in single and binary systems: experimental study and physicochemical interpretation of the adsorption mechanism. Chem. Eng. J. 389, 124467. https://doi.org/10.1016/j.cej.2020.124467.

Liu, H., Long, L., Weng, X., Zheng, S., Xu, Z., 2020a. Efficient removal of tetrabromobisphenol A using microporous and mesoporous carbons: the role of pore structure. Microporous Mesoporous Mater. 298, 110052. https://doi.org/10.1016/j.micromeso.2020.110052.

Maazinejad, B., Mohammadnia, O., Ali, G.A.M., Makhlouf, A.S.H., Nadagouda, M.N., Sillanpää, M., Asiri, A.M., Agarwal, S., Gupta, V.K., Sadegh, H., 2020. Taguchi L9 (34) orthogonal array study based on methylene blue removal by single-walled carbon nanotubes-amine: adsorption optimization using the experimental design method, kinetics, equilibrium and thermodynamics. J. Mol. Liq. 298, 112001. https://doi.org/10.1016/j.molliq.2019.112001.

Maddodi, S.A., Alalwan, H.A., Alminshid, A.H., Abbas, M.N., 2020. Isotherm and computational fluid dynamics analysis of nickel ion adsorption from aqueous solution using activated carbon. S. Afr. J. Chem. Eng. 32, 5–12. https://doi.org/10.1016/j.sajce.2020.01.002.

Malekimoghadam, R., 2018. 3 – Carbon Nanotubes Processing, Carbon Nanotube-Reinforced Polymers. Elsevier Inc. https://doi.org/10.1016/B978-0-323-48221-9.00003-0.

Miyah, Y., Lahrichi, A., Idrissi, M., Khalil, A., Zerrouq, F., 2018. Adsorption of methylene blue dye from aqueous solutions onto walnut shells powder: equilibrium and kinetic studies. Surfaces and Interfaces 11, 74–81. https://doi.org/10.1016/j.surfin.2018.03.006.

Mohamed, M.G., Atayde, E.C., Matsagar, B.M., Na, J., Yamauchi, Y., Wu, K.C.W., Kuo, S.W., 2020. Construction hierarchically mesoporous/microporous materials based on block copolymer and covalent organic framework. J. Taiwan Inst. Chem. Eng. 1–13. https://doi.org/10.1016/j.jtice.2020.06.013.

Mohamed, S.K., Alazhary, A.M., Al-Zaqri, N., Alsalme, A., Alharthi, F.A., Hamdy, M.S., 2019. Cost-effective adsorbent from arabinogalactan and pectin of cactus pear peels: kinetics and thermodynamics studies. Int. J. Biol. Macromol. https://doi.org/10.1016/j.ijbiomac.2019.11.187.

Mojaver, P., Khalilarya, S., Chitsaz, A., Assadi, M., 2020. Multi-objective optimization of a power generation system based SOFC using Taguchi/AHP/TOPSIS triple method. Sustain. Energy Technol. Assessments 38, 100674. https://doi.org/10.1016/j.seta.2020.100674.

Mousavi, S.V., Bozorgian, A., Mokhtari, N., Gabris, M.A., Rashidi Nodeh, H., Wan

Ibrahim, W.A., 2019. A novel cyanopropylsilane-functionalized titanium oxide magnetic nanoparticle for the adsorption of nickel and lead ions from industrial wastewater: Equilibrium, kinetic and thermodynamic studies. Microchem. J. 145, 914–920. https://doi.org/10.1016/j.microc.2018.11.048.

Neris, J.B., Luzardo, F.H.M., da Silva, E.G.P., Velasco, F.G., 2019. Evaluation of adsorption processes of metal ions in multi-element aqueous systems by lignocellulosic adsorbents applying different isotherms: a critical review. Chem. Eng. J. 357, 404–420. https://doi.org/10.1016/j.cej.2018.09.125.

Oh, W. Da, Lee, M.G.H., Chanaka Udayanga, W.D., Veksha, A., Bao, Y., Giannis, A., Lim, J.W., Lisak, G., 2019. Insights into the single and binary adsorption of copper(II) and nickel(II) on hexagonal boron nitride: performance and mechanistic studies. J. Environ. Chem. Eng. 7, 102872. https://doi.org/10.1016/j.jece.2018.102872.

Oh, W. Da, Wong, Z., Chen, X., Lin, K.Y.A., Veksha, A., Lisak, G., He, C., Lim, T.T., 2020. Enhanced activation of peroxydisulfate by CuO decorated on hexagonal boron nitride for bisphenol A removal. Chem. Eng. J. 393, 124714. https://doi.org/10.1016/j.cej.2020.124714.

Peigney, A., Laurent, C., Flahaut, E., Bacsa, R.R., Rousset, A., 2001. Specific surface area of carbon nanotubes and bundles of carbon nanotubes. Carbon N. Y. 39, 507–514. https://doi.org/10.1016/S0008-6223(00)00155-X.

Pereira, K.A.B., Cestari, S.P., Cucinelli Neto, R.P., Macedo, K.R.M., Mendes, L.C., 2019. Oxidized-sulfonated multi-walled carbon nanotube/hydroxyapatite hybrid particles: synthesis and characterization. J. Solid State Chem. 279, 120924. https://doi.org/10.1016/j.jssc.2019.120924.

Qu, J., Tian, X., Jiang, Z., Cao, B., Akindolie, M.S., Hu, Q., Feng, C., Feng, Y., Meng, X., Zhang, Y., 2020. Multi-component adsorption of Pb(II), Cd(II) and Ni(II) onto microwave-functionalized cellulose: kinetics, isotherms, thermodynamics, mechanisms and application for electroplating wastewater purification. J. Hazard Mater. 387 https://doi.org/10.1016/j.jhazmat.2019.121718.

Sahithi, V.V.D., Malayadri, T., Srilatha, N., 2019. Optimization of turning parameters on surface roughness based on taguchi technique. Mater. Today Proc. 18, 3657–3666. https://doi.org/10.1016/j.matpr.2019.07.299.

Sellaoui, L., Mendoza-Castillo, D.I., Reynel-Ávila, H.E., Ávila-Camacho, B.A., Díaz-Muñoz, L.L., Ghalla, H., Bonilla-Petriciolet, A., Lamine, A. Ben, 2019. Understanding the adsorption of Pb2+, Hg2+ and Zn2+ from aqueous solution on a lignocellulosic biomass char using advanced statistical physics models and density functional theory simulations. Chem. Eng. J. 365, 305–316. https://doi.org/10.1016/j.cej.2019.02.052.

Su, Q., Yang, S., He, Y., Qin, Z., Cui, X., 2020. Prepared self-growing supported nickel catalyst by recovering Ni (II) from metal wastewater using geopolymer microspheres. J. Hazard Mater. 389, 121919. https://doi.org/10.1016/j.jhazmat.2019.121919.

Tang, S., Yang, J., Lin, L., Peng, K., Chen, Y., Jin, S., Yao, W., 2020. Construction of physically crosslinked chitosan/sodium alginate/calcium ion double-network hydrogel and its application to heavy metal ions removal. Chem. Eng. J. 124728 https://doi.org/10.1016/j.cej.2020.124728.

Torres, D., Pinilla, J.L., Suelves, I., 2017. Unzipping of multi-wall carbon nanotubes with different diameter distributions: effect on few-layer graphene oxide obtention. Appl. Surf. Sci. 424, 101–110. https://doi.org/10.1016/j.apsusc.2017.01.273.

US EPA, 2012. US environmental protection agency: 2012 edition of the drinking water standards and health advisories. 2012. In: Drink. Water Stand. Heal. Advis. 2–6 https://doi.org/EPA 822-S-12-001.

WHO, 2017. Guidelines for Drinking-Water Quality. https://doi.org/10.1016/S1462-0758(00)00006-6. Fourth Ed. 631.

Wu, S.L., Chen, C.M., Kuo, J.H., Wey, M.Y., 2020. Synthesis of carbon nanotubes with controllable diameter by chemical vapor deposition of methane using Fe@Al2O3 core–shell nanocomposites. Chem. Eng. Sci. 217, 115541. https://doi.org/10.1016/j.ces.2020.115541.

Yang, F., Jiang, Q., Xie, W., Zhang, Y., 2017. Effects of multi-walled carbon nanotubes with various diameters on bacterial cellular membranes: cytotoxicity and adaptive mechanisms. Chemosphere 185, 162–170. https://doi.org/10.1016/j.chemosphere.2017.07.010.

Yang, Y., Zhang, H., Yan, Y., 2019. Synthesis of CNTs on stainless steel microfibrous composite by CVD: effect of synthesis condition on carbon nanotube growth and structure. Compos. B Eng. 160, 369–383. https://doi.org/10.1016/j.compositesb.2018.12.100.

Yatom, S., Selinsky, R.S., Koel, B.E., Raitses, Y., 2017. "Synthesis-on" and "synthesis-off" modes of carbon arc operation during synthesis of carbon nanotubes. Carbon N. Y. 125, 336–343. https://doi.org/10.1016/j.carbon.2017.09.034.

Ye, X., E, S., Fan, M., 2019. The influences of functionalized carbon nanotubes as lubricating additives: length and diameter. Diam. Relat. Mater. 100, 107548. https://doi.org/10.1016/j.diamond.2019.107548.

Zhang, Y., Wang, Y., Zhang, H., Li, Y., Zhang, Z., Zhang, W., 2020. Recycling spent lithium-ion battery as adsorbents to remove aqueous heavy metals: adsorption kinetics, isotherms, and regeneration assessment. Resour. Conserv. Recycl. 156, 104688. https://doi.org/10.1016/j.resconrec.2020.104688.

Zhao, L.X., Liang, J.L., Li, N., Xiao, H., Chen, L.Z., Zhao, R.S., 2020. Kinetic, thermodynamic and isotherm investigations of Cu2+ and Zn2+ adsorption on Li[sbnd]Al hydrotalcite-like compound. Sci. Total Environ. 716 https://doi.org/10.1016/j.scitotenv.2020.137120.

Zhao, X., Chang, S., Long, J., Li, J., Li, X., Cao, Y., 2019. The toxicity of multi-walled carbon nanotubes (MWCNTs) to human endothelial cells: the influence of diameters of MWCNTs. Food Chem. Toxicol. 126, 169–177. https://doi.org/10.1016/j.fct.2019.02.026.